



HAL
open science

TBC1D32 variants disrupt retinal ciliogenesis and cause retinitis pigmentosa

Béatrice Bocquet, Caroline Borday, Nejla Erkilic, Daria Mamaeva, Alicia Donval, Christel Masson-Garcia, Karine Parain, Karolina Kaminska, Mathieu Quinodoz, Irene Perea-Romero, et al.

► To cite this version:

Béatrice Bocquet, Caroline Borday, Nejla Erkilic, Daria Mamaeva, Alicia Donval, et al.. TBC1D32 variants disrupt retinal ciliogenesis and cause retinitis pigmentosa. JCI Insight, 2023, 8 (21), pp.e169426. 10.1172/jci.insight.169426 . hal-04229192

HAL Id: hal-04229192

<https://hal.science/hal-04229192>

Submitted on 5 Oct 2023

HAL is a multi-disciplinary open access archive for the deposit and dissemination of scientific research documents, whether they are published or not. The documents may come from teaching and research institutions in France or abroad, or from public or private research centers.

L'archive ouverte pluridisciplinaire **HAL**, est destinée au dépôt et à la diffusion de documents scientifiques de niveau recherche, publiés ou non, émanant des établissements d'enseignement et de recherche français ou étrangers, des laboratoires publics ou privés.



Distributed under a Creative Commons Attribution 4.0 International License

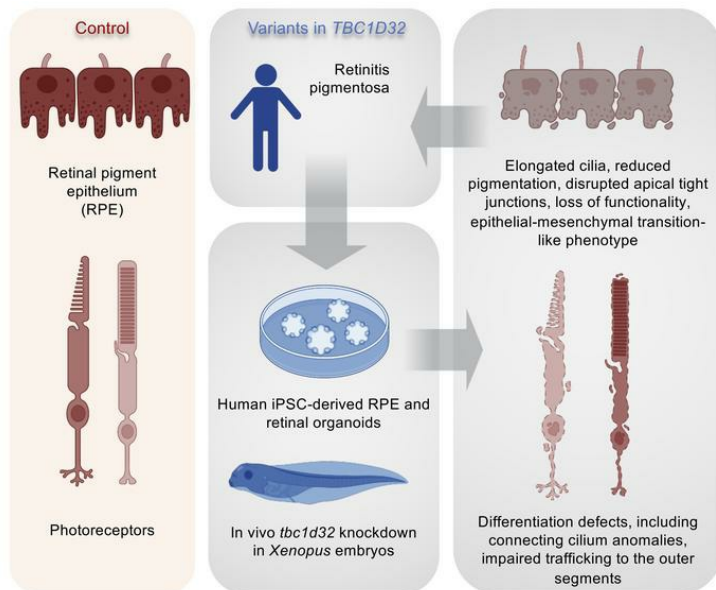
TBC1D32 variants disrupt retinal ciliogenesis and cause retinitis pigmentosa

Béatrice Bocquet, ... , Muriel Perron, Vasiliki Kalatzis

JCI Insight. 2023. <https://doi.org/10.1172/jci.insight.169426>.

Research In-Press Preview Genetics Ophthalmology

Graphical abstract



Find the latest version:

<https://jci.me/169426/pdf>



1 ***TBC1D32* variants disrupt retinal ciliogenesis and cause retinitis pigmentosa**

2
3 Béatrice Bocquet^{1,2,#,*}, Caroline Borday^{3,#}, Nejla Erkilic^{1,2,#}, Daria Mamaeva^{1,#}, Alicia Donval³, Christel
4 Masson-Garcia³, Karine Parain³, Karolina Kaminska^{4,5}, Mathieu Quinodoz^{4,5,6}, Irene Perea-Romero^{7,8},
5 Gema Garcia-Garcia^{8,9,10}, Carla Jimenez-Medina¹, Hassan Boukhaddaoui¹, Arthur Coget^{11,12}, Nicolas
6 Leboucq¹¹, Giacomo Calzetti^{4,5,13}, Stefano Gandolfi¹³, Antonio Percesepe¹³, Valeria Barili¹³, Vera Uliana¹⁴,
7 Marco Delsante¹⁵, Francesca Bozzetti¹⁶, Hendrik PN Scholl^{4,5}, Marta Corton^{7,8}, Carmen Ayuso^{7,8}, José M.
8 Millan^{8,9,10}, Carlo Rivolta^{4,5,6}, Isabelle Meunier^{1,2,§}, Muriel Perron^{3,§,*}, and Vasiliki Kalatzis^{1,§,*}

9
10 ¹Institute for Neurosciences of Montpellier (INM), University of Montpellier, Inserm, Montpellier, France

11 ²National Reference Centre for Inherited Sensory Diseases, University of Montpellier, CHU, Montpellier,
12 France

13 ³Université Paris-Saclay, CNRS, Institut des Neurosciences Paris-Saclay, Saclay, France

14 ⁴Institute of Molecular and Clinical Ophthalmology Basel (IOB), Basel, Switzerland

15 ⁵Department of Ophthalmology, University of Basel, Basel, Switzerland

16 ⁶Department of Genetics and Genome Biology, University of Leicester, Leicester, UK

17 ⁷Department of Genetics, Health Research Institute-Fundación Jiménez Díaz University Hospital,
18 Universidad Autónoma de Madrid (IIS-FJD, UAM), Madrid, Spain

19 ⁸Center for Biomedical Network Research on Rare Diseases (CIBERER), Instituto de Salud Carlos III,
20 Madrid, Spain

21 ⁹Molecular, Cellular and Genomics Biomedicine Research Group, Instituto de Investigación Sanitaria La
22 Fe (IIS La Fe), Valencia, Spain

23 ¹⁰Joint Unit of Rare Diseases, IIS La Fe-Centro de Investigación Príncipe Felipe, Valencia, Spain

24 ¹¹Department of Neuroradiology, University of Montpellier, CHU, Montpellier, France

25 ¹²Institute for Human Functional Imaging (I2FH), University of Montpellier, CHU, Montpellier, France

26 ¹³Department of Medicine and Surgery, University Hospital of Parma, Parma, Italy

27 ¹⁴Department of Medical Genetics, University Hospital of Parma, Parma, Italy

28 ¹⁵Department of Nephrology, University Hospital of Parma, Parma, Italy

29 ¹⁶Neuroradiology Unit, Diagnostic Department, University Hospital of Parma, Parma, Italy

30
31 # These authors contributed equally to this work

32 § These authors contributed equally to this work

33 *Authors for correspondence:

34 Beatrice Bocquet

35 CRMR Maolya
36 Hôpital Gui de Chauliac
37 80 Ave Augustin Fliche
38 34295 Montpellier
39 France
40 Phone: +33 4 67 33 69 74
41 Email: beatrice.bocquet@inserm.fr
42
43 Muriel Perron
44 Paris-Saclay Institute of Neuroscience
45 Campus CEA Saclay
46 Bâtiment 151
47 91400 Saclay
48 France
49 Phone: +33 1 69 82 60 92
50 Email: muriel.perron@universite-paris-saclay.fr
51
52 Vasiliki Kalatzis
53 INM, Inserm U1298
54 Hôpital St Eloi, BP 74103
55 80 Ave Augustin Fliche
56 34091 Montpellier
57 France
58 Phone: +33 4 99 63 60 76
59 Email: vasiliki.kalatzis@inserm.fr
60
61

62 **Abstract (<200 words)**

63 Retinitis pigmentosa (RP) is the most common inherited retinal disease (IRD) and is characterized
64 by photoreceptor degeneration and progressive loss of vision. We report here four patients who presented
65 with RP from three unrelated families with variants in *TBC1D32*, which to date has never been associated
66 with an IRD. To validate *TBC1D32* as a putative RP causative gene, we combined *Xenopus* in vivo
67 approaches and human iPSC-derived retinal models. Our data showed that *TBC1D32* was expressed during
68 retinal development and that it played an important role in retinal pigment epithelium (RPE) differentiation.
69 Furthermore, we identified a role for *TBC1D32* in ciliogenesis of the RPE. We demonstrated elongated
70 ciliary defects that resulted in disrupted apical tight junctions, loss of functionality (delayed retinoid cycling
71 and altered secretion balance), and the onset of an epithelial-mesenchymal transition-like phenotype. Lastly,
72 our results also suggested photoreceptor differentiation defects, including connecting cilium anomalies, that
73 resulted in impaired trafficking to the outer segment in both cones and rods in *TBC1D32* iPSC-derived
74 retinal organoids. Overall, our data not only highlight a critical role for *TBC1D32* in the retina but
75 demonstrate that *TBC1D32* mutations lead to RP. We thus identify *TBC1D32* as an IRD causative gene.

76

77 **Keywords**

78 *TBC1D32/Bromi*; retinitis pigmentosa; RPE; primary cilium; epithelial-mesenchymal transition (EMT);
79 *Xenopus*; induced-pluripotent stem cells (iPSCs); retinal organoids

80

81

82 **Introduction**

83 Inherited retinal diseases (IRDs) are a group of clinically and genetically heterogeneous disorders
84 characterized by a dysfunction or degeneration of the light-sensing cells of the retina, the photoreceptors,
85 and/or their underlying support tissue, the retinal pigment epithelium (RPE) (1). In the majority of cases,
86 IRDs are associated with a progressive loss of vision that can have a variable age of onset and severity of
87 symptoms. Although each disease is monogenic, there are >270 known causative genes
88 (<https://sph.uth.edu/retnet>). The most common IRD is a rod-cone dystrophy known as retinitis pigmentosa
89 (RP) (2), characterized by night blindness appearing in childhood and followed by a progressive loss of
90 peripheral vision. There are >90 causative RP genes with a collective prevalence of 1/4000 (3) and with
91 autosomal dominant, autosomal recessive or X-linked modes of transmission (4). Furthermore, mutations
92 in the same gene can give rise to either isolated RP or RP associated with extra-retinal symptoms.

93 The clinical heterogeneity associated with RP is partly explained by the diverse localizations and
94 roles of the proteins encoded by the causative genes within the retina (5). The photoreceptors have a unique
95 morphology comprising an axon, nucleus-containing cell body, a mitochondria-rich inner segment (IS) and
96 an outer segment (OS) filled with lipid disks where the phototransduction process is initiated following
97 light interaction. The IS is connected to the OS by a highly modified primary cilium called the connecting
98 cilium (CC). The genes responsible for isolated RP can be divided into groups that play key roles in the cell
99 body (splicing, transcription, development), IS (transport, signaling) or OS (structure, phototransduction)
100 (3, 5). The genes for syndromic RP are mostly localized at the level of the CC or the periciliary membrane
101 complex (6). These diseases are also known as ciliopathies and, although they can give rise to isolated RP,
102 retinal defects are often linked to defects in other ciliated tissues (7). Interestingly, the RPE also contains a
103 primary cilium on its apical side, which is critical for RPE maturation and homeostasis maintenance (8),
104 and RPE ciliary defects were recently associated with retinal ciliopathies (9).

105 Currently, the genetic causes in ~40% of RP patients remain unknown (4). In order to resolve such
106 cases, we performed whole exome sequencing (WES) in the probands from three unrelated families
107 presenting clinically with autosomal recessive RP and identified previously undescribed biallelic variants
108 in *TBC1D32* (OMIM: 615867). *TBC1D32* belongs to a family of Rab GTPase-activating proteins (GAPs)
109 containing a Tre-2, Bub-2, and Cdc16 (TBC) domain. *TBC1D32* has been shown to have a role in regulating
110 the structure of the primary cilium in the neural tube (10). Zebrafish *tbc1d32* morphants showed a curvature
111 of the body axis and hydrocephalus and a *Tbc1d32* knock-out mouse model exhibited neural patterning
112 defects comprising, exencephaly, preaxial polydactyly as well as poorly developed eyes. Accordingly,
113 recessive loss-of-function *TBC1D32* variants were reported as responsible for Oral-Facial-Digital (OFD)
114 syndrome type IX (OMIM: 258865), a ciliopathy characterized by defects in the development of the oral
115 cavity, face and digits, associated with microphthalmia/anophthalmia (11). However, OFD syndrome is not

116 classically associated with retinal anomalies, and the *TBC1D32* animal models do not have reported retinal
117 defects.

118 Therefore, to validate *TBC1D32* as a putative RP causative gene, we combined animal and human
119 disease modeling by (i) performing hypomorphic knockdowns in an in vivo *Xenopus* model and (ii)
120 generating iPSC-derived RPE and retinal organoids from an RP patient carrying *TBC1D32* variants.
121 Together, our data show that *TBC1D32* is expressed during retinal development and plays an important role
122 in ciliogenesis. The disruption of *TBC1D32* results in abnormal RPE maturation and function, as well as
123 defective photoreceptor differentiation and OS trafficking. Overall, we identify *TBC1D32* as an IRD
124 causative gene, which has implications for alleviating current diagnostic deadlocks.
125

126 **Results**

127 **Three unrelated families present with clinical features of RP**

128 Four patients from 3 unrelated families (Patient 1, Family 1; Patient 2, Family 2; Patients 3 and 4,
129 Family 3) were studied ([Supplemental Figure 1](#)) and their ocular data are summarized in [Supplemental](#)
130 [Table 1](#). Night blindness occurred in childhood (Patients 1 and 2) or in early adulthood (Patients 3 and 4).
131 Refraction errors were highly variable, the two patients older than 50 years were legally blind. Peripheral
132 visual field impairment occurred early in the second decade with a severe impairment after the age of 50
133 years. Beyond the classic signs of RP noted on multimodal imaging and on spectral-domain optical
134 coherence tomography (SD-OCT), all patients shared abnormal visibility of large choroidal vessels in the
135 entire peripheral retina suggesting RPE loss with photoreceptor degeneration ([Figure 1](#)). None of the
136 patients had documented macular edema. On full-field electroretinogram recordings, none of the patients
137 had discernable rod and cone responses (data not shown). The patients did not mention any systemic
138 symptoms, and consistently a systemic check-up only revealed mild MRI anomalies with an atrophic aspect
139 of the superior vermis in patients 1 and 2 ([Supplemental Figure 2](#)). In addition, Patient 2 was diagnosed at
140 27 years of age with non-proteinuric chronic kidney disease. Urinary protein-to-creatinine and albumin-to-
141 creatinine ratios were 0.19 and 0.10 g/g, respectively, with no notable urinary sediment. Autoimmunity
142 markers were negative and C3 and C4 complement fractions, and IgG, IgA and IgM plasmatic levels, were
143 normal. Kidneys were bilaterally reduced (95 mm) and showed mild cortical hyperechogenicity with a few
144 bilateral cortical and parapelvic cysts (max 9 mm). Negative genetic testing for *PKD1* and *PKD2* genes
145 further ruled out polycystic kidney disease.

146

147 ***TBC1D32* pathogenic variants segregate with the RP in three families**

148 Trio WES was performed on the Patient 1 and his healthy parents ([Supplemental Figure 1A](#)). No
149 mutation in genes previously associated with syndromic and non-syndromic RP (<https://sph.uth.edu/retnet/>)
150 was detected. We identified two variants in the *TBC1D32* gene (NM_001367760.1) in trans in the proband,
151 one of which was carried by each parent. The maternal intron 2 variant c.317+5G>A was predicted to
152 probably alter splicing according to Human Splicing Finder and described at a frequency of 0.000004092
153 in the gnomAD database (<https://gnomad.broadinstitute.org/>). To ascertain pathogenicity, we performed
154 RT-PCR amplification of exons 1 to 5 on whole blood cells (WBCs) and detected two bands in the proband
155 and maternal samples, the smaller of which corresponded to in-frame skipping of exon 2 ([Supplemental](#)
156 [Figure 1D](#)). The paternal variant, c.846delTCCTA; p.(Asn282Lysfs*7) (exon 7), was absent from the
157 gnomAD database, and was predicted to induce a frameshift and the introduction of a premature termination
158 codon (PTC).

159 WES performed for Patient 2 (Supplemental Figure 1B) showed that he was compound heterozygous
160 for the variants c.18_27del; p.(Ser6Argfs*8) in exon 1 (maternal allele) and c.1141-1G>A in intron 10
161 (paternal allele). Both variants were absent from databases. The second variant was predicted to strongly
162 alter splicing according to an in silico prediction software (<https://mobidetails.iurc.montp.inserm.fr/MD>).
163 To confirm its pathogenicity, we performed RT-PCR amplification of exons 9 to 13 on WBCs of the patient
164 and his father, and detected as many as seven additional splicing events that bore PTCs and were not present
165 in the control (Supplemental Figure 1E).

166 Trio WES was performed on Patients 3 and 4, and a healthy sister (Supplemental Figure 1C). The
167 affected siblings were compound heterozygous for the variants c.1267G>T; p.(Glu423*) in exon 12, and
168 c.3513G>T; p.(Trp1171Cys) in exon 31, whereas the unaffected sister was heterozygous for the c.3513G>T
169 variant. The frequency in gnomAD of the c.1267G>T and c.3513G>T variants were 0.0000124 (described
170 three times in the database) and 0.00000402 (described once), respectively. The missense variant is situated
171 in the carboxy-terminal Rab GAP TBC domain, in a highly conserved position relative to the orthologous
172 proteins (Supplemental Figure 1F). The in silico pathogenicity scores were ambiguous
173 (<https://varsome.com/>). Structural analysis using AlphaFold showed that the Tryptophan at position 1171
174 was located at the beginning of an alpha helix, and its substitution by a Cysteine residue was likely to create
175 a steric hindrance with a Tyrosine at position 1019. However, with a CADD pathogenicity score of 31
176 (<https://cadd.gs.washington.edu/>), this variant was classed as of unknown significance according to the
177 ACMG classification. Taken together, the probands of all three families carried biallelic *TBC1D32* variants,
178 of which only one allele could be predicted as loss of function.

179

180 ***tbc1d32* is expressed in the neuroretina and RPE during *Xenopus* development**

181 As *TBC1D32* variants were never previously linked to RP, we used a *Xenopus laevis* model, which
182 is highly suited to functional development and gene knockdown studies (12), to test the expression and role
183 of *tbc1d32* in the retina. *Xenopus tbc1d32* is located on chromosome 5L, displays an exon/intron structure
184 identical to the human homologue (33 exons), and is predicted to encode a 1297 aa protein with ~60%
185 identity to human TBC1D32 (accession # NM_001367759.1 or NM_001367760.1 or NM_152730.6). We
186 cloned the *Xenopus tbc1d32* full-length coding sequence (Supplemental Figure 3) and analyzed its
187 expression during development (Figure 2A). *tbc1d32* transcripts were first detected at stage 25 (13) in
188 multiciliated epithelial cells in the epidermis and in the optic vesicle. From stage 27-28, expression was
189 also detected in the otic vesicle, the brain, and the pronephric nephrostomes. We further analyzed the
190 expression of *tbc1d32*, and *indian hedgehog (ihh)* as an RPE marker (14), on retinal sections using an
191 RNAscope fluorescent multiplex assay (Figure 2B). At stage 25, *tbc1d32* was expressed in all progenitor
192 cells of the optic vesicle. At stage 27-28, transcripts were abundantly detected in the presumptive neural

193 retina, but only a few molecules were detected in the presumptive RPE, labelled with *ihh*. At stages 32-33,
194 *tbc1d32* transcripts were clearly visible in the developing RPE, with a peak at stage 35-36. From stage 37-
195 38 onwards, *tbc1d32* expression decreased in the RPE, the inner nuclear, and ganglion cell layers but
196 remained well expressed in the outer nuclear layer (ONL) containing the photoreceptors, where it decreased
197 at later stages. Finally, we confirmed the presence of *tbc1d32* transcripts in RPE cells by qPCR on mRNAs
198 from dissected RPE at stage 35-36 (Figure 2C). In conclusion, in the retina, *tbc1d32* is expressed in retinal
199 progenitors, developing photoreceptors and RPE cells, consistent with a putative role in retinogenesis.

200

201 **Knockdown of *Xenopus tbc1d32* leads to developmental RPE and photoreceptor defects**

202 To determine the impact of *tbc1d32* knockdown in retinal development, we designed two different
203 morpholinos (Mo1 and Mo2) that we injected at the 4-cell stage in one blastomere giving rise to neural
204 ectoderm (Figure 3, A and B, and Supplemental Figures 3 and 4). This led to a unilateral *tbc1d32*
205 knockdown mainly limited to neural tissues (Supplemental Figure 4). A high dose (20 ng) of either Mo1 or
206 Mo2 led to severe developmental defects, including curvature of the body axis and
207 microphthalmia/anophthalmia of the injected embryos (data not shown). No discernable eye malformations
208 were observed upon injection of a control Mo.

209 As we suspected hypomorphic pathogenicity in *TBC1D32* patients, we tested lower doses of *tbc1d32*
210 Mo. At a dose of 10 or 15 ng of Mo1, *Xenopus* embryos no longer displayed a microphthalmic phenotype,
211 and we did not detect retinal toxicity using a cell death assay (Supplemental Figure 5). By contrast,
212 morphant embryos exhibited retinal pigmentation defects, comprising a decreased intensity and
213 discontinuity in pigmentation on retinal sections compared to controls (Figure 3C). This phenotype was
214 similar upon Mo2 injection (Supplemental Figure 6A) and was partially restored upon co-injection with
215 Mo-resistant *tbc1d32* mRNAs (i.e. not recognized by the Mo), demonstrating its specificity (Figure 3C).
216 We further analyzed actin cytoskeleton organization in RPE cells by phalloidin staining of dissected eyes
217 injected with Mo1 or Mo2 (Figure 3D and Supplemental Figure 6B). In controls, phalloidin staining was
218 uniform, outlining cell membranes and highlighting the typical hexagonal shape of RPE cells, whereas the
219 staining was heterogeneous and irregular in *tbc1d32* morphants, highlighting an altered shape of RPE cells.
220 We hence investigated the impact of *tbc1d32* knockdown on RPE differentiation using *mitf* and *ihh* as RPE
221 markers (14). Using in situ hybridization, we found that their expression was significantly decreased in the
222 retinas of embryos injected with Mo1 or Mo2 compared to controls (Figure 4, A-D and Supplemental Figure
223 7A and B). This decrease was confirmed by qPCR (Supplemental Figure 8). Importantly, this effect was
224 partially rescued upon co-injection with Mo-resistant *tbc1d32* mRNAs (Supplemental Figure 9).
225 Collectively, these data suggest a key role for *tbc1d32* in RPE differentiation.

226 We also explored whether photoreceptor development was affected upon *tbc1d32* knockdown. By
227 immunofluorescence (IF) at stage 41, when photoreceptors are well-differentiated, we found that the vast
228 majority of morphant retinas injected with 10 ng of Mo1 exhibited normal labeling in the ONL of both
229 Rhodopsin and S/M cone Opsin (Figure 4D). By contrast, at a higher dose of 15 ng, around half of the
230 morphant embryos showed reduced staining. To determine whether these defects arise early during
231 photoreceptor differentiation, we assessed *rhodopsin* expression at stage 35-36, when *rhodopsin* RNA
232 begins to be detected. We found significantly reduced staining in *tbc1d32* morphant retinas compared to
233 controls (Figure 4E), which was confirmed following Mo2 injections (Supplemental Figure 7C). Taken
234 together, *tbc1d32* knockdown results in RPE defects, while photoreceptors are affected in a dose-dependent
235 manner, being either largely preserved or exhibiting obvious differentiation defects.

236

237 ***Xenopus* RPE ciliogenesis is affected upon *tbc1d32* knockdown**

238 Defects in primary cilia morphology, namely curled cilia, were reported in both neural progenitor
239 cells of *Tbc1d32*^{-/-} mouse embryos and in renal tubules of zebrafish *tbc1d32* morphants (10). Consistently,
240 by staining with the widely used cilium markers Arl13b (ciliary shaft marker) and γ -Tubulin (basal body
241 marker), we detected ciliogenesis defects in neural tube cells of *Xenopus tbc1d32* morphants, which
242 displayed longer primary cilia than controls (Figure 5, A and B). We thus assayed if the RPE developmental
243 defects in the *tbc1d32* morphants were also associated with ciliogenesis defects. As primary cilia are
244 necessary for the maturation of mouse RPE but then disappear in fully differentiated cells (15), we first
245 characterized the developmental window during *Xenopus* retinogenesis when the RPE cilia were present.
246 We used both the RPE marker Otx2, to delineate cells, and acetylated α -Tubulin and γ -Tub, to label primary
247 cilia. First, we verified that acetylated α -Tubulin co-localized with Arl13b along the cilium and with γ -Tub
248 at the basal body level, confirming that it is a reliable marker of the *Xenopus* RPE cilium (Figure 5C). We
249 detected ciliated RPE cells in the presumptive retina from stage 27-28. The percentage of ciliated cells
250 increased and peaked at stage 35, and then decreased from stage 37-38 onwards (Figure 5, D and E). In
251 *tbc1d32* morphant retinas of stage 35 embryos, the mean cilia length was significantly higher than in control
252 retinas (Figure 5, F and G; Supplemental Figure 10, A and B). We then analyzed photoreceptor ciliogenesis
253 and found a significant decrease in the number of photoreceptors showing Arl13b staining in *tbc1d32*
254 morphant retinas compared to controls (Figure 5, H and I and Supplemental Figure 10, C and D). In
255 conclusion, *tbc1d32* knockdown impacted ciliogenesis in both *Xenopus* RPE and photoreceptor cells.

256

257 **Human *TBC1D32* fibroblasts display a primary cilium defect**

258 Human fibroblasts have long constituted a classical screening assay for ciliary defects (16).
259 Therefore, we cultured fibroblasts from a skin biopsy of Patient 1 to better study the expression of both

260 mutant *TBC1D32* alleles and their impact on ciliogenesis. Using primers specific to exons 1 and 8 to assay
261 the c.317+5G>A allele, we detected a 931-bp band in control cells and three bands in the patient cells
262 (Supplemental Figure 11A): the first was similar in size to the control band but contained the last 18 bp of
263 intron 2 (Supplemental Figure 11B) that introduced a PTC; the second and most predominant was 769 bp
264 and corresponded to the in-frame skipping of exon 2 (Supplemental Figure 11C), as observed in patient
265 WBCs; the third was 591 bp and corresponded to the skipping of exons 2 and 3 that also introduced a PTC
266 (Supplemental Figure 11D). Thus, only transcript 2 was predicted to lead to translation, which corroborated
267 our observations in WBCs, despite the less comprehensive analysis in this cell type. Using primers specific
268 to exons 6 and 11 to assay the c.846delTCCTA allele, we detected an ~600-bp amplicon in control and
269 patient cells (Supplemental Figure 11E), the latter of which contained a transcript with the 5-bp deletion in
270 exon 7 (Supplemental Figure 11F) that introduced a PTC. These results suggested that the mutant transcript
271 did not undergo nonsense-mediated decay, which was consistent with the qPCR results showing similar
272 levels of *TBC1D32* expression in both control and patient fibroblasts (Supplemental Figure 11G).

273 We then assayed ciliogenesis by IF studies of ARL13B with the axoneme markers acetylated α -
274 tubulin and polyglutamylated tubulin (GT335), and the basal body marker pericentrin (PCN), which is
275 present in both the mother and daughter centrosomes (17). We detected a similar spatial distribution
276 between control and *TBC1D32* fibroblasts (Figure 6, A-F). By contrast, and consistent with the *Xenopus*
277 data, we detected a significantly elongated ARL13B-labelled cilium in the patient cells compared to
278 controls (Figure 6, A-G). We also assayed intraflagellar transport (IFT) by IF studies of IFT88 (18, 19),
279 which correctly extended beyond acetylated α -tubulin at both ends of the cilium in control and patient cells
280 (Figure 6, H and I). Lastly, consistent with the qPCR data, we clearly detected *TBC1D32* using an antibody
281 specific to an epitope encoded by exons 24 to 28 (Supplemental Figure 11G). *TBC1D32* was located basal
282 to acetylated α -tubulin in control and patient fibroblasts (Figure 6, J and K), where it overlapped with PCN
283 (Figure 6, L-O). Taken together, *TBC1D32* localized to the centrosomes of the primary cilium in human
284 fibroblasts, and mutant *TBC1D32* proteins led to elongation defects.

285

286 ***TBC1D32* iPSC-derived RPE has an elongated cilium and disrupted tight junctions**

287 To unravel the pathophysiology associated with *TBC1D32* mutations, we reprogrammed the
288 fibroblasts of Patient 1 into induced pluripotent stem cells (iPSCs) to subsequently generate highly relevant
289 human retinal models. Two *TBC1D32* iPSC lines were confirmed as pluripotent by the expression of the
290 host pluripotency markers (Supplemental Figure 12, A and B) and germline markers following an embryoid
291 body (EB) differentiation assay (Supplemental Figure 12C). In addition, we confirmed genomic stability
292 by testing the copy number of the recombination hotspots in iPSCs (20) (Supplemental Figure 12D).
293 Interestingly, in contrast to the fibroblast data, *TBC1D32* expression levels in the two patient iPSC lines

294 were lower than in control cells (Supplemental Figure 12E). Lastly, we confirmed the presence of the
295 causative *TBC1D32* mutations c.317+5G>A in exon 2 and c.846delTCCTA in exon 7 in the patient iPSC
296 lines by Sanger sequencing (Supplemental Figure 12F).

297 We then differentiated the patient and control lines into iPSC-derived RPE. Due to the different qPCR
298 profiles observed between fibroblasts and iPSCs, we assayed *TBC1D32* expression in the iPSC-derived
299 RPE and detected lower levels in the patient RPE compared to controls (Supplemental Figure 13A), further
300 suggesting tissue-specific regulation. By IF analysis, *TBC1D32* partially co-localized with PCN in control
301 and patient iPSC-derived RPE, as in primary fibroblasts, but the staining intensity was lower in the patient
302 RPE (Supplemental Figure 13, B and C), consistent with the qPCR results. We then assayed the morphology
303 of the *TBC1D32* iPSC-derived RPE from 12 weeks post-seeding. Co-labelling of the apical tight junction
304 marker ZO1 and ARL13B demonstrated a regular cobblestone morphology and primary cilium staining for
305 the control RPE (Figure 7A). By contrast, the morphology of the *TBC1D32* patient iPSC-derived RPE was
306 highly irregular with cilia significantly longer than controls (Figure 7, B and C). Furthermore, we detected
307 gaps between cells, and ZO1 aggregates at the contact points of multiple cells, in the *TBC1D32* RPE that
308 were absent from control RPE (Figure 7, D and E). The disrupted tight junctions were confirmed by trans-
309 epithelial resistance (TER) measurements, which steadily decreased in the *TBC1D32* RPE from 6 weeks
310 post-seeding to levels significantly lower than control RPE at 13 weeks (Figure 7F). In conclusion, the
311 *TBC1D32* patient iPSC-derived RPE presented with a primary cilium defect and disrupted apical tight
312 junctions.

313

314 ***TBC1D32* iPSC-derived RPE displays an EMT-like phenotype**

315 Primary cilium defects in RPE reportedly provoke an EMT-like phenotype, characterized initially by
316 a loss of tight junctions (21). We thus assayed the *TBC1D32* RPE for signs of cytoskeletal changes
317 associated with EMT by testing the expression of vimentin and SMA (22) (Figure 8, A-D). A low and
318 relatively regular intensity of vimentin expression was detected in the control iPSC-derived RPE, whereas
319 islands of upregulated expression were detected in the patient RPE, which were associated with a loss of
320 MERTK expression, further confirming the loss of RPE identity. Similarly, large and abundant SMA-
321 positive islands were detected in the *TBC1D32* iPSC-derived RPE, compared to controls, which were
322 associated with disrupted ZO1 expression (Supplemental Figure 13, D-F). Thus, the disrupted apical
323 junctions in the *TBC1D32* iPSC-derived RPE were accompanied by a transition to a mesenchymal state.

324 These observations were further confirmed by gene expression levels of other EMT markers (Figure
325 8, E-I). The genes encoding the adherens junction markers E-cadherin (*CDH1*), P-cadherin (*CDH3*) and β -
326 catenin (*CTNNB1*) showed reduced expression levels in the *TBC1D32* RPE, compared to controls,
327 confirming the loss of epithelial cell-cell contacts. Furthermore, the transcription factor SNAIL (*SNAI1*),

328 which mediates EMT, and Fibronectin 1 (*FNI*), a marker of EMT, showed increased expression levels.
329 Consistently, western blot analysis of E- and P-cadherin showed significantly decreased levels in the patient
330 RPE compared to controls (Figure 8, J and K). In contrast to the qPCR data, β -catenin showed similar levels
331 in control and patient RPE (Figure 8L). We thus analyzed its subcellular distribution and showed that it was
332 predominately localized to the membrane fraction in control RPE and to the cytosolic fraction in the patient
333 RPE (Figure 8M). This difference was consistent with the release of β -catenin from the membrane, which
334 allows it to act as a transcriptional activator of EMT genes, such as *SNAIL* (23). Taken together, the
335 *TBC1D32* iPSC-derived RPE displays altered morphology and deregulated expression profiles that are
336 hallmarks of EMT activation.

337

338 ***TBC1D32* iPSC-derived RPE shows altered functionality**

339 The loss of tight and adherens junctions reportedly affects the apical-basal polarity of RPE with an
340 impact on functionality (21). Hence, we assayed the expression of CRALBP, an RPE marker and actor of
341 the visual cycle, together with N-cadherin, an adherens junction and EMT marker (22) (Figure 9, A and B).
342 We detected a regular membrane staining of N-cadherin in control RPE compared to notable patches of
343 discontinuous N-cadherin staining in the patient RPE. Similarly, we detected reduced CRALBP staining at
344 the membrane and an increased signal in the cytosol in the patient RPE compared to controls. This shift
345 was confirmed by western blot analyses (Figure 9C). Furthermore, the most pronounced areas of CRALBP
346 staining showed reduced N-cadherin levels. Moreover, we detected a decrease in expression of the
347 corresponding gene, *RLBPI*, as well as other visual cycle genes, *LRAT* and *RPE65* in *TBC1D32* RPE
348 compared to controls (Supplemental Figure 13, G-I). *ABCA4*, which is involved in the visual cycle in
349 photoreceptors, was recently described to be also expressed in the RPE (24) and, accordingly, its expression
350 was also reduced in the patient RPE (Supplemental Figure 13J).

351 To determine whether the differential expression of these visual cycle actors in the patient RPE
352 impacted its function, we assayed for the accumulation of retinoids, detectable as lipid droplets termed
353 retinosomes (25) by transmission electron microscopy (TEM). We detected an accumulation of lipid
354 droplets in the *TBC1D32* RPE as compared to controls (Figure 9, D-F), which were identified as
355 retinosomes by the specific marker perilipin-2 (Figure 9G). The significant abundance of retinosomes
356 prompted us to assay the polarized secretion of the angiogenic factors pigment epithelium-derived factor
357 (PEDF) and VEGF, another key RPE function, by ELISA (26). We detected a significant increase in apical,
358 and a significant decrease in basal, PEDF and VEGF secretion in the *TBC1D32* RPE, as compared to
359 controls (Figure 9H). Taken together, the cellular changes in the *TBC1D32* RPE result in disrupted retinoid
360 cycling and altered secretion balance.

361

362 ***TBC1D32* iPSC-derived retinal organoids show defective trafficking to outer segments**

363 As photoreceptors possess a specialized cilium, the CC, we assayed whether *TBC1D32* defects also
364 led to photoreceptor anomalies in iPSC-derived retinal organoids (27). Bright-field imaging showed that
365 control and *TBC1D32* organoids had a similar morphology with a brush border (Figure 10, A and B)
366 containing IS and OS-like structures and a distinct lamina corresponding to the ONL (Figure 10, C and D).
367 This organization was confirmed by IF studies of CRX and recoverin (RCVRN), although staining was
368 visibly reduced in the patient organoids (Figure 10, E and F). Furthermore, we assayed the expression of
369 ZO1 and CRALBP, markers of the outer limiting membrane (OLM) formed by the end feet of Müller glial
370 cells. The OLM was clearly discernible by the co-localized CRALBP/ZO1 signals in the control organoids,
371 whereas we detected only a faint CRALBP signal and no ZO1 signal in the *TBC1D32* organoids (Figure
372 10, G and H). Moreover, co-staining of ZO1 and rhodopsin kinase (RK) showed that RK expression
373 extended beyond the OLM into the IS/OS layer in control organoids but not as far in the *TBC1D32*
374 organoids (Figure 10, I and J). We thus investigated the CC by assaying the expression of ARL13B in
375 parallel to rhodopsin (RHO). In control organoids, ARL13B was visible as punctate dots close to the ONL
376 with RHO extended beyond into the OS, whereas, in *TBC1D32* organoids, ARL13B was only faintly
377 discernible and RHO remained close to the ONL (Figure 10, K and L). The RK and RHO expression profiles
378 suggested that trafficking to the OS was impaired, thus we tested the expression of the cone and rod OS
379 marker ABCA4 and the rod-specific OS marker PDE6B. ABCA4 and PDE6B staining was clearly
380 detectable in the OS of the control organoids but visibly reduced in the *TBC1D32* organoids (Figure 10, M
381 and N). In addition, arrestin 3 (ARR3)-positive cones of varying lengths were identified in the control
382 organoids, a subset of which co-expressed the more mature R/G opsin cone marker (Figure 10O). By
383 comparison, the cones in the *TBC1D32* organoids appeared stunted with a distinctly visible co-localization
384 signal at the edge of the cells beyond the ONL (Figure 10P). In conclusion, in addition to affecting the RPE,
385 *TBC1D32* variants directly affect photoreceptors at the level of the CC and result in impaired trafficking to
386 the OS in both cones and rods.

387 **Discussion**

388 With the technological advancements of next-generation sequencing, the genetic diagnosis yield of
389 IRDs had considerably increased over the last ten years (28). However, recently, the slope of the
390 identification curve has reached a plateau (<https://sph.uth.edu/retnet>), raising challenges for genetic
391 counselling and therapeutic opportunities for patients. Furthermore, the genetic landscape for IRDs is
392 complexifying, as it becomes increasingly evident that mutations in the same gene can give rise to
393 differential phenotypes or even clinically distinct disorders (29). *TBCID32* is now another perfect example
394 of the breakdown in borders between disorders. To date, *TBCID32* variants were only associated with OFD
395 syndrome, a severe malformative disorder. However, here, we report pathogenic *TBCID32* variants in four
396 patients from three independent families presenting clinically with RP. Furthermore, by combining an in
397 vivo *Xenopus* model and human iPSC-derived retinal models, we describe a critical role for *TBCID32* in
398 retinal differentiation and ciliogenesis, and demonstrate that reduced *TBCID32* levels impact the RPE and
399 photoreceptors. We thus identify *TBCID32* as a causative IRD gene.

400 OFD syndromes form a rare subgroup of ciliopathies characterized by oral cavity, facial and digital
401 anomalies with or without heart defects, polycystic kidney disease, or corpus callosum agenesis (30). There
402 is a high clinical heterogeneity linked to sixteen causative genes. The most frequent is the X-linked *OFDI*,
403 which encodes a centrosomal protein. Interestingly, rare *OFDI* patients have been described as presenting
404 with non-syndromic retinal degeneration (31), suggesting that variants in other *OFD* genes may also give
405 rise to IRDs. In 2014, loss-of-function *TBCID32* variants were first described as associated with the OFD
406 syndrome type IX (11). Clinical symptoms ranged from midline cleft, anophthalmia, and polydactyly to
407 choanal atresia, agenesis of corpus callum, vermis and pituitary hypoplasia, and hydrocephalus.
408 Subsequently, seven patients from five families were reported as carrying different pathogenic *TBCID32*
409 variants and presenting with syndromic ciliopathies (32). It is noteworthy that one patient from a Finnish
410 family with compound heterozygous indels in *TBCID32* also exhibited a progressive retinal dystrophy but
411 this was not further explored (33).

412 Taking into account the clinical data in relation to age, none of the patients reported here showed
413 signs of *TBCID32*-related OFD syndrome. It should be noted, though, that MRI revealed mild subclinical
414 alterations, which suggests that *TBCID32* variants may give rise to a disease spectrum with a certain
415 threshold for the appearance of clinical signs. It is likely that type or severity of the associated variant
416 accounts for this spectrum. We now raise the number of identified pathogenic *TBCID32* variants, identified
417 in eight unrelated families, to ten: one missense (c.3513G>T), two nonsense (c.1267G>T; c.3724C>T),
418 three splicing (c.317+5G>A; c.1141-1G>A; c.1372+1G>T) and four indels (c.18_27del; c.846delTCCT;
419 c.1165_1166dup; c.2151del) ((32-34) and this study). Although it is possible that nonsense and indel
420 *TBCID32* variants result in loss of function, splicing and missense variants are more ambiguous.

421 The c.317+5G>A splicing variant, carried by Patient 1 in trans to a frameshift indel, only results in
422 mild RP, which is likely explained by the resulting in-frame exon skipping that may result in a shorter
423 partially functional protein. Similarly, the c.1141-1G>A variant, carried by Patient 2 in trans to a frameshift
424 indel, which promotes the creation of multiple aberrant splicing variants also did not result in severe
425 syndromic disease. However, this patient presented with additional renal defects, which were possibly of a
426 ciliopathic nature. An association between altered ciliary function and the development of renal cysts has
427 been linked to variants in the ciliary function-related genes *PKD1/PKD2* (35). Patient 2 was negative for
428 pathogenic *PKD1/PKD2* variants, raising the possibility that the renal anomalies may be due to the
429 *TBCID32* variants. This is supported by the zebrafish *tbc1d32* morphant model that shows dose-dependent
430 ciliary defects in the distal kidney tubules (10), and the association of renal anomalies with other ciliopathies
431 (7). Along this line, a recent study described developmental cochlear defects in the knockout *Tbc1d32*
432 mouse model (36), and we also detected *tbc1d32* in the *Xenopus* otic vesicle, suggesting that *TBCID32*
433 variants may also provoke ciliopathies with deafness associated. Finally, the mildest *TBCID32*-associated
434 phenotype reported to date is the later onset RP in Patients 3 and 4 carrying the missense c.3513G>T variant
435 in trans to a nonsense variant. The predicted structural changes associated with this variant suggest the
436 production of a mutant protein, which we hypothesise may be partially functional to account for the
437 moderate phenotype. Taken together, and in consideration of the dose-dependent phenotypic severity in the
438 *Xenopus tbc1d32* morphants, we propose that hypomorphic *TBCID32* variants give rise to RP and loss-of-
439 function variants to OFD syndrome.

440 Pertinently, none of the patients showed ocular malformations, whereas they all presented with
441 features of retinal degeneration that were compatible with both RPE and photoreceptor defects. This clinical
442 data is strongly supported by our functional data. Firstly, the phenotypes of the *Xenopus tbc1d32* morphants
443 and the human *TBCID32* iPSC-derived RPE models highlighted RPE differentiation defects that affected
444 functionality. Most notably, the slowing down of retinoid recycling, as evidenced by retinosome
445 accumulation, is reminiscent of the RPE defect associated with mutations in the visual cycle protein *RPE65*,
446 which causes Leber congenital amaurosis (37). Visual cycle disruption reduces the availability of 11 *cis*-
447 retinol, which subsequently impacts the phototransduction process causing visual impairment. Secondly,
448 the *Xenopus* morphants and iPSC-derived retinal organoids showed photoreceptor differentiation anomalies
449 and disturbed trafficking of photoreceptor proteins to the OS, which would affect their function. In addition,
450 the disrupted apical VEGF secretion identified in the *TBCID32* iPSC-derived RPE, would also impact
451 neurodevelopment and photoreceptor protection throughout life (38), further impacting phototransduction
452 and vision.

453 The disrupted ciliogenesis of the RPE and photoreceptors in both the *Xenopus* and human models
454 leads us to propose that *TBCID32*-associated RP is a retinal ciliopathy (7). In particular, we show that

455 TBC1D32 defects result in elongated primary cilia in fibroblasts, neural tube and RPE cells. Ciliary length
456 is determined by an interplay between ciliary assembly and disassembly processes, which rely on an
457 effective bidirectional IFT system (39). There have been examples in the past of gene variants associated
458 with retinal degeneration that result in elongated cilia. For example, variants in the gene encoding IFT172,
459 have been associated with non-syndromic or syndromic forms of RP (40, 41) and elongated cilia were
460 detected on patient's fibroblasts (41). Similarly, variants in the gene encoding the transition zone protein
461 CEP290 (42), associated with the early onset retinal dystrophy Leber congenital amaurosis (LCA), resulted
462 in elongated primary cilia on patient fibroblasts (43) Furthermore, these fibroblasts showed normal IFT88
463 distribution, similar to our observations on *TBC1D32* cells, indicating that anterograde IFT was normal.
464 Finally, variants in the gene encoding NPHP5/IQCB1 also associated with LCA were recently shown to
465 provoke elongated primary cilia in patient-derived fibroblasts and iPSC-derived RPE (44), further
466 confirming that elongated ciliary defects give rise to retinal ciliopathies.

467 Importantly, we show that the tight junction defects of the *TBC1D32* RPE were associated with an
468 EMT-like phenotype both at the mRNA and protein levels. We did observe a slight discrepancy for β -
469 catenin, as the decreased mRNA levels did not corroborate with the unchanged protein levels. The
470 regulation of β -catenin in EMT, however, is highly complex due to the protein's dual roles in adhesion and
471 transcription and the interplay between these pools has not been elucidated (45). Nonetheless, we showed
472 that there was a release of β -catenin into the cytosol, which would increase the transcriptionally active pool
473 consistent with EMT (23). We can thus only speculate that, at the time of analysis, the RPE was in a dynamic
474 EMT state and that feedback regulations on mRNA or protein levels were in process. *TBC1D32* is an actor
475 of the Hedgehog (HH) pathway in primary cilia, which acts to regulate the GLI family of transcription
476 factors (46). *TBC1D32* controls the HH pathway by allowing GLI proteins to be properly localized in the
477 primary cilia and correctly activated in response to high-level HH signaling (10). In cancer cells, it has been
478 shown that activated GLI proteins bind and transcribe genes that control EMT (namely *SNAIL*) among other
479 cell processes (47). Therefore, our data suggest that ciliary elongation in the RPE due to *TBC1D32*
480 disruption may cause HH signaling perturbations, which would activate EMT causing a loss of identity and
481 function. Although beyond the scope of this manuscript, future studies should be aimed at precisely
482 deciphering the link between *TBC1D32*, HH signaling, and EMT in the retina. Lastly, a similar link between
483 primary ciliary defects and EMT in the RPE was also made in a murine model of the syndromic retinal
484 ciliopathy Bardet-Biedl syndrome (*BBS8^{-/-}*), where an EMT-like phenotype was associated with defective
485 cellular polarization and morphology (21), further validating our observations.

486 In general, the proteins encoded by OFD genes have been attributed to three functional modules in
487 primary cilia: centriole elongation, transition zone, and intraflagellar transport (30). *TBC1D32* was
488 attributed to the elongation module as zebrafish *tbc1d32* interacts with cell cycle-related kinase to regulate

489 ciliary membrane and axonemal growth in the neural tube (10) and murine *Tbc1d32* acts redundantly with
490 the centrosomal protein *Dzip11* to regulate ciliogenesis (48). We now demonstrate that *TBC1D32* also
491 regulates ciliogenesis in the retina in human and *Xenopus* models. Consistent with the fact that *TBC1D32*
492 is not associated with the intraflagellar transport module, we did not detect abnormal IFT88 distribution in
493 *TBC1D32* fibroblasts. Interestingly though, IFT88 pooling was previously reported in the fibroblasts of the
494 *TBC1D32*-associated OFD type IX patient (19) and in a *TBC1D32* knockout hTERT-RPE1 cell line (49).
495 Furthermore, the murine *tbc1d32*^{-/-} and zebrafish morphant models displayed curled axonemes enveloped
496 by dilated ciliary membranes (10), in contrast to the elongated ciliary defect that we report here in the
497 *Xenopus* knockdown model and in the *TBC1D32* patient cells. These differences could be due to a dose-
498 dependent effect related to the amount of remaining functional *TBC1D32* protein. Thus, taken together, we
499 propose that the severity of *TBC1D32* disruption will lead to phenotypic variability at the level of the
500 primary cilium and an ensuing disease spectrum.

501 In conclusion, we identify *TBC1D32* as an IRD gene responsible for RP and broaden the clinical
502 spectrum associated with *TBC1D32* variants. As we identified pathogenic variants in multiple unrelated
503 families and, as one of the probands also presented with renal anomalies, we highly recommend that
504 *TBC1D32* be added to the list of candidate genes to be screened for both isolated and syndromic RP.

505 **Methods**

506 **Clinical investigations**

507 Patients underwent a comprehensive ophthalmological examination (best-corrected visual acuity,
508 kinetic visual field, SD-OCT, short-wavelength fundus autofluorescence (SW-FAF), color fundus
509 photography and full-field electroretinography performed in accordance with the guidelines of the
510 International Society for Electrophysiology of Vision). Age of onset, initial symptoms and extra-ocular
511 manifestations were also reviewed. The systemic check-up included a cerebral MRI, hypothalamic-pituitary
512 hormone dosages, skeletal investigations, ear, nose, throat heart and kidney evaluations.

513

514 **Whole exome sequencing and bioinformatic analyses**

515 Targeted exome sequencing library preparation, exome capture, sequencing and data analysis for
516 Patient 1 and his unaffected parents were performed by IntegraGen SA (Evry, France) using Sureselect All
517 Exon V5 (Agilent Technologies) on an Illumina HiSeq4000, as previously described (50). WES for Patient
518 2 was performed using the Twist Comprehensive Exome Panel (Twist bioscience) and sequenced on a
519 HiSeq 4000 instrument (Illumina) with an average coverage of 100–120X at each nucleotide position. WES
520 for Patients 3 and 4 and a healthy sibling was conducted at CNAG-CRG (Centro Nacional de Análisis
521 Genómico, Barcelona, Spain) using Sureselect All Exon V5 (Agilent Technologies) and captured libraries
522 were paired-end (2x100 bp) sequenced on Illumina HiSeq2000 platform. For Patients 2 to 4, BWA
523 (V0.7.17) was used for mapping raw reads to the human genome reference sequence (build hg19) and the
524 bioinformatic analysis was performed as described (51). For Patients 3 and 4, the raw genomic data was
525 processed in parallel through the RD-Connect analysis pipeline in the centralized RD-Connect database
526 (52).

527

528 ***Xenopus* embryo collection, RNA extraction and cloning**

529 *Xenopus laevis* embryos were obtained from TEFOR (Paris-Saclay) by conventional methods of
530 hormone-induced egg laying and in vitro fertilization, staged according to Nieuwkoop and Faber's table of
531 development (13). Total RNA from wild-type *Xenopus laevis* embryos was isolated using the Nucleospin
532 RNA XS kit (Macherey Nagel). Following reverse transcription, PCR amplification was performed using
533 specific primers (Supplemental Table 2) designed from the *tbc1d32* sequence in the National Center for
534 Biology Information (NCBI) *Xenopus laevis* EST database (accession # XM_041562734.1). The amplified
535 *tbc1d32* sequence was then cloned using the ligation-free cloning system in the XhoI-linearized pCS2+
536 plasmid (E001, ABM) and verified by sequencing (Supplemental Figure 3).

537

538 ***Xenopus* whole-mount *in situ* hybridization**

539 Digoxigenin-labeled antisense RNA probes were generated according to the manufacturer's
540 instruction (Roche) from gifted plasmids: pBS-*ihh* (Stephen Ekker, Mayo Clinic, Minnesota, USA);
541 pGEM-Teasy-*mitf* (Andrea Viczian, Upstate Medical University, New York, USA); pGEM-T-*rhodopsin*
542 (Thomas Hollemann, Martin-Luther-University Halle-Wittenberg, Halle, Germany). The *tbc1d32* probe
543 was generated from the entire *tbc1d32* coding region cloned into pCS2+. Whole-mount *in situ*
544 hybridizations were carried out as described (14) and analyzed on 50 µm vibratome transverse sections.

545

546 **RNAscope *in situ* hybridization**

547 *Xenopus* embryos were fixed in 4% PFA at 4°C for 24 h, embedded in OCT and sectioned at 10 µm
548 thickness on a cryostat (Leica). The RNAscope Multiplex Fluorescent 2.0 Assay was performed according
549 to the manufacturer's protocols using the HyBEZ oven. Opal 520 and 570 dyes were applied to slides along
550 with DAPI counterstain.

551

552 **Morpholinos and Microinjection**

553 Translation-blocking antisense Morpholino oligonucleotides (GeneTools) are listed in [Supplemental](#)
554 [Table 2](#). Five nL microinjections were performed at the four-cell stage into one of the two blastomeres
555 giving rise to the neural ectoderm. 500 pg of *tbc1d32* mRNA (synthesized with mMessage mMachin kit,
556 Life Technologies) and/or 10 to 20 ng of *tbc1d32* Mo1 or Mo2 were injected; a standard Mo (GeneTools)
557 was injected as a control. For each condition, mRNA encoding GFP was co-injected as a lineage tracer.
558 The efficacy of the two *tbc1d32* Mo was tested by analysing *in vivo* GFP fluorescence following co-
559 injection of a chimeric GFP construct fused downstream of the Mo-complementary sequence
560 ([Supplemental Figure 4](#)).

561

562 **Fibroblasts and iPSCs**

563 Control fibroblast and iPSCs lines were previously reported (53). The skin biopsy of Patient 1 was
564 performed at the National Reference Center for Inherited Sensory Diseases (Montpellier, France). Dermal
565 fibroblasts were reprogrammed using the CytoTune-iPS 2.0 Sendai Reprogramming Kit (Thermo Fisher
566 Scientific), and iPSC colonies cultured in Essential 8 Medium (Gibco) (54). Trilineage differentiation
567 potential was determined by an EB differentiation assay as described (54). Genomic stability of iPSCs was
568 analyzed using droplet digital qPCR analysis by Stem Genomics (Montpellier, France). iPSC genomic DNA
569 was isolated, PCR amplified using *TBC1D32*-specific primers ([Supplemental Table 3](#)), and the amplicons
570 sequenced on an Applied Biosystems 3130xL or SeqStudio genetic analyzer (54).

571

572 **iPSC-derived RPE and retinal organoids**

573 iPSC-derived RPE was differentiated (53) and cryostored at passage 2 (26) as described. All
574 experiments were performed on passage 3 RPE seeded on Matrigel-coated translucent Corning cell culture
575 inserts with high-density 0.4 μM pores (BD Falcon). The TER of 4 independent inserts at each time point
576 was measured using the Epithelial Volt/Ohm Meter EVOM2 (Word Precision Instruments) and expressed
577 as an average value in Ω/cm^2 (53). The TEM analysis of iPSC-derived RPE grown on transwell inserts was
578 performed as described (53). Retinal organoids were differentiated from adherent iPSCs and cultured as
579 free-floating structures in DMEM/F12+GlutaMAX (Gibco) supplemented with taurine and retinoic acid,
580 as described (27).

581

582 **RT-PCR and qPCR**

583 Total *Xenopus* RNA from at least 12 optic vesicles at stage 30, 12 whole retinas, 40 dissected RPE,
584 or 40 neural retinas at stage 35-36, was extracted using trizol and Nucleospin RNA Kit (Macherey Nagel).
585 cDNA was synthesized from 290 ng of RNA with Superscript IV (Invitrogen). For qPCR experiments, 10
586 ng of cDNA was amplified in triplicate using SsoFast EvaGreen Supermix (BioRad) on a C1000 thermal
587 cycler (CFX96 real-time system, BioRad). Quantification was performed using the $\Delta\Delta\text{Ct}$ method, and levels
588 were normalized to *odc*, *ef1a*, and *rpl8* and expressed relative to control Mo or neural retina. Total human
589 RNA was extracted from WBCs, fibroblasts, iPSCs, and iPSC-derived RPE using the PAXgene RNA kit
590 (BD Biosciences), Tempus Spin RNA Isolation kit (Applied Biosystems), or RNeasy Mini Kit (Qiagen).
591 cDNA was synthesized from 500 ng of RNA with the SuperScript III First-Strand Synthesis System using
592 random hexamers (Life Technologies) or from 2 μg of RNA with the High Capacity cDNA Reverse
593 Transcription Kit (Applied Biosystems). RT-PCR amplification of Patient 1's WBCs and fibroblasts was
594 performed using AmpliTaq Gold 360 Master Mix (Applied Biosystems) and Patient 2's WBCs using
595 GoTaq G2 DNA Polymerase (Promega). Amplicons were either gel purified and directly sequenced (WBC
596 Patient 1), or subcloned into pGEMTeasy vectors and then sequenced. For qPCR experiments, a 1/10
597 (iPSCs) or a 1/20 dilution (RPE) of the cDNA was amplified in triplicate using the FastStart SYBR Green
598 Master mix on a LightCycler 480 II thermal cycler (Roche). Quantification was performed using the $\Delta\Delta\text{Ct}$
599 method normalized to *GAPDH*, and levels expressed relative to control. Experiments were duplicated using
600 a second housekeeping gene. Primer sequences are presented in [Supplemental Table 4](#).

601

602 **Immunofluorescence studies**

603 *Xenopus* embryos were fixed in 4% paraformaldehyde (PFA) and immunolabelling was performed
604 on paraffin sections with antibodies listed in [Supplemental Table 5](#) using standard procedures. Antigen
605 retrieval was performed by boiling the sections in 10 mM sodium citrate and 0.05% Tween-20 for 9 min.
606 For cilia analysis, sections were bleached in 10% H_2O_2 in PBS at 55°C. Nuclei were stained with Hoechst

607 (Sigma-Aldrich). Sections were imaged with a Zeiss M2 microscope, or a Zeiss LSM 710 confocal
608 microscope for cilia analysis, and processed with Zen software (Zeiss). For phalloidin staining, dissected
609 eyes were fixed in 4% PFA and labelled with Alexa Fluor 568-phalloidin (1/40, Molecular Probes). IF
610 studies of human fibroblasts, iPSCs, EBs, RPE and retinal organoids were performed as previously
611 described (53-55). Primary antibodies were incubated at 4°C overnight and secondary antibodies with 0.2
612 µg/ml Hoechst 33258 (Sigma-Aldrich) were incubated at room temperature for 1 h ([Supplemental Table](#)
613 [6](#)). Samples were imaged using a Zeiss ApoTome 2 Upright wide-field microscope or Confocal LSM700
614 microscope.

615

616 **Image quantification**

617 All *Xenopus* experiments were performed at least in duplicate and results from one representative
618 experiment are shown. To quantify activated caspase³⁺ labeled cells, 6 to 9 sections per retina were analyzed
619 using Adobe Photoshop CS4 software. *In situ* hybridization staining integrated density in eyes or in retinal
620 sections was measured in the delineated region of interest using Fiji software (<https://fiji.sc/>). Fiji software
621 was also used to quantify *tbc1d32* expression upon RNAscope *in situ* hybridization. To image and measure
622 cilia lengths, Z-stacks of 11 µm retina sections were taken with 0.3 µm steps and converted into single
623 planes by maximum projection with Fiji software. For each condition, the length of 3 to 8 cilia per retina
624 was quantified on image stacks using the ObjectJ plugin (<https://sils.fnwi.uva.nl/bcb/objectj/>). The
625 quantification of the cilium lengths in human fibroblasts and iPSC-derived RPE were performed using
626 Image J and Imaris Software (Bitplane), respectively. For the RPE, five random regions of a transwell filter
627 were measured. The quantification of the SMA area was performed on a montage of 16 regions of a
628 transwell filter using the Imaris Software. The quantification of the lipid vesicles in the TEM images was
629 performed manually.

630

631 **Western blot analyses**

632 Unless otherwise stated, hiPSC-derived RPE cells were seeded on inserts, scraped 12 weeks post-
633 seeding, resuspended in Laemmli sample buffer containing 2-mercaptoethanol, and western blot analysis
634 performed as previously described (53). The Mem-PERTM Plus Kit (Thermo Scientific) was used to
635 separate the cytosolic and membrane fractions prior to mixing with Laemmli buffer. Primary and secondary
636 antibodies ([Supplemental Table 6](#)) were incubated overnight at 4°C or 45 min at room temperature,
637 respectively. Fluorescence were detected using the ODYSSEY CLx imaging system (LI-COR) and
638 quantified with the Image Studio Lite software.

639

640 **Secretion assays**

641 VEGF and PEDF secretion of human iPSC-derived RPE was assayed by ELISA (R&D Systems) on
642 24 h conditioned media collected from the apical and basolateral chambers of the cultured inserts as
643 described (26). Samples were collected from 16 to 19 inserts and assayed in triplicate. The mean
644 concentration values of the *TBC1D32* samples were expressed as a percentage of the control values.

645

646 **Statistical analyses**

647 Statistical analyses were performed using the two-tailed Mann and Whitney test, unpaired two-
648 tailed Student's t-test, or the Fisher's exact test with GraphPad Prism 8.3 software. The number of samples
649 per experiment and condition is indicated in the corresponding figures and legends. For all analyses, a P
650 value less than 0.05 was considered significant.

651

652 **Study approval**

653 Clinical and genetic analyses were performed after signed informed consent using approved
654 protocols of the Montpellier University Hospital, France (ID n°: IRB-MTP_2021_11_202100959), the
655 Research Ethics Committee of the Fundación Jiménez Díaz University Hospital, Madrid, Spain (ID n°: CM
656 06-2016 FJD), the Research Ethics Committee of the University Hospital La Fe, Valencia, Spain (ID n°:
657 2019/0098) and the Institute of Molecular and Clinical Ophthalmology Basel (ID n°: 2019-01660), and in
658 agreement with the Declaration of Helsinki. Skin biopsies and iPSC reprogramming were approved by the
659 French National Agency for the Safety of Medicines and Health Products (ID n°: 2014-A00549-38).
660 *Xenopus* care followed institutional guidelines (licenses A91272108 and C 91-471-102) and study protocols
661 were approved by the institutional animal care committee CEEA #59 and the Direction Départementale de
662 la Protection des Populations (APAFIS #21474-2019071210549691v2 and #32589-
663 2021072719047904v4).

664

665 **Data availability**

666 All data are available in the main text or the supplementary materials. Data point values for all graphs are
667 found in the Supporting Data Values file.

668

669 **Author contributions**

670 The authorship order among co-first was determined by the chronological order that they began
671 working on the project. BB, CB, NE, DM, IM, MP and VK designed research studies. BB, CB, NE, DM,
672 AD, KP, CMG, KK, MQ, IPR and MC conducted experiments. CJM and HB analysed data. GGG, AC,
673 NL, GC, SG, AP, VB, VU, MD, FB, HPNS, CA, JMM, IM performed clinical investigations. CB, CA,
674 JMM, CR, IM, MP, VK performed supervision. BB, CB, IM, MP, VK wrote the manuscript. All authors
675 reviewed and edited the manuscript.

676

677 **Acknowledgements**

678 This work is dedicated to Pr. Christian Hamel who initiated the study, identified *TBC1D32* as the
679 potential candidate gene, and passed away prematurely in 2017. We thank L. Surcouf, J. Guillot, T. Crouzet-
680 Deprost, M. Pegart and K. Damodar for technical assistance; M. Le Quintrec Donnette for helpful
681 discussions; L. Mansard for variant classification; C. Sanjurjo-Soriano, J. Roger and C.-M. Dhaenens for
682 critical reading of the manuscript; C. Fabre for EMT discussions; C. Cazevaille of the INM CoMET
683 electron microscopy facility; P. Clair of the high-debit qPCR platform (qPHD, Univ Montpellier); the MRI
684 Imaging platform, and the CNAG-CRG for assistance with WES. This work was funded by: Fondation de
685 France, Fondation Valentin Haüy and the associations Retina France (MP), France Choroideremia (VK),
686 AVIESAN-UNADEV (VK, MP) and IRRP (BB and IM); Swiss National Science Foundation (grant n°
687 176097 and 204285) (CR); BBMRI-LPC 2016 access call for Whole Exome Sequencing (FP7/2007-2013,
688 grant agreement n° 313010) (CA); Instituto de Salud Carlos III (Spain) (PI19/00321, PI19/00303 and
689 FI17/00192) (CA and JMM); IIS-FJD BioBank (PT13/0010/0012) (CA); Comunidad de Madrid (CAM,
690 RAREGenomics Project, B2017/BMD-3721) (CA); Organización Nacional de Ciegos Españoles (ONCE)
691 (CA); University Chair UAM-IIS-FJD of Genomic Medicine (CA); Centro de Investigación Biomédica en
692 Red Enfermedades Raras (CIBERER, 06/07/0036) (CA), and European Regional Development Fund
693 (FEDER) (CA). The RD-Connect Genome Phenome Analysis platform was developed under a FP7/2007-
694 2013-funded project (grant agreement n° 305444; CA). CMG is supported by Retina France. BB, CA, JM,
695 CR, IM and VK are members of the European Retinal Disease Consortium (ERDC).

696

697

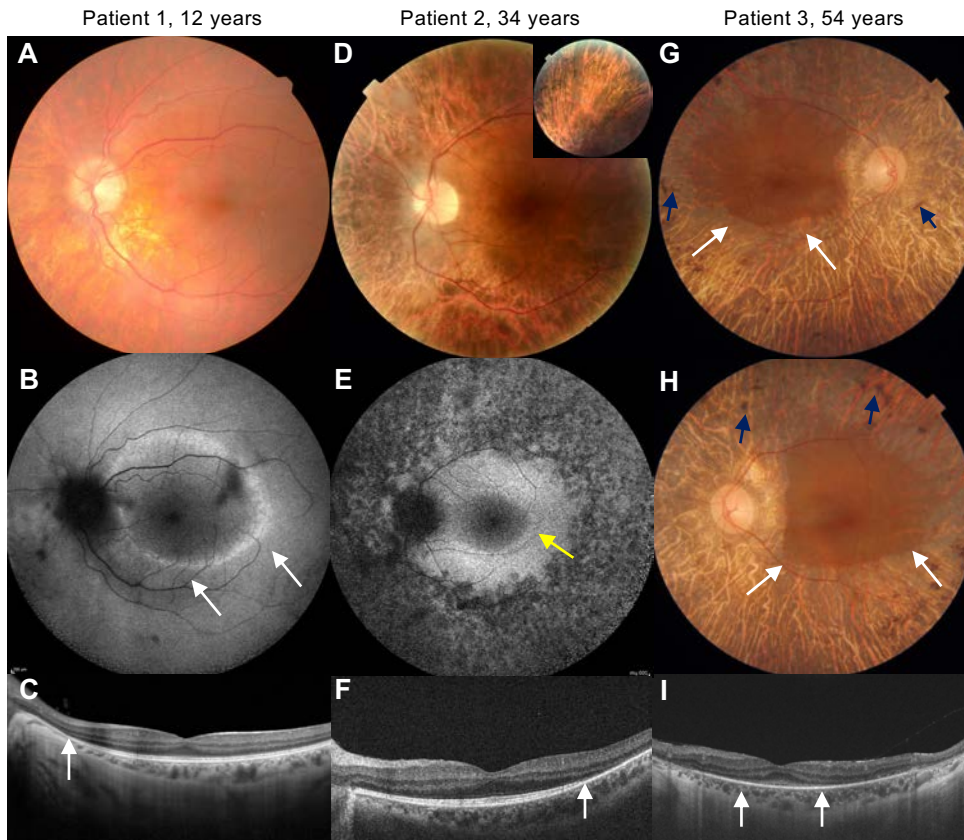
699 **References**

- 700 1. Berger W, et al. The molecular basis of human retinal and vitreoretinal diseases. *Prog Retin Eye Res.* 2010;29(5):335-75.
701
702 2. Hanany M, et al. Worldwide carrier frequency and genetic prevalence of autosomal recessive inherited
703 retinal diseases. *Proc Natl Acad Sci U S A.* 2020;117(5):2710-6.
704 3. Verbakel SK, et al. Non-syndromic retinitis pigmentosa. *Prog Retin Eye Res.* 2018;66:157-86.
705 4. Dias MF, et al. Molecular genetics and emerging therapies for retinitis pigmentosa: Basic research and
706 clinical perspectives. *Prog Retin Eye Res.* 2018;63:107-31.
707 5. Hamel CP. Gene discovery and prevalence in inherited retinal dystrophies. *C R Biol.* 2014;337(3):160-
708 6.
709 6. Bachmann-Gagescu R, Neuhauss SC. The photoreceptor cilium and its diseases. *Curr Opin Genet Dev.*
710 2019;56:22-33.
711 7. Bujakowska KM, et al. Photoreceptor Cilia and Retinal Ciliopathies. *Cold Spring Harb Perspect Biol.*
712 2017;9(10).
713 8. Sun C, et al. Primary cilia in retinal pigment epithelium development and diseases. *J Cell Mol Med.*
714 2021;25(19):9084-8.
715 9. May-Simera HL, et al. Primary Cilium-Mediated Retinal Pigment Epithelium Maturation Is Disrupted
716 in Ciliopathy Patient Cells. *Cell Rep.* 2018;22(1):189-205.
717 10. Ko HW, et al. Broad-minded links cell cycle-related kinase to cilia assembly and hedgehog signal
718 transduction. *Dev Cell.* 2010;18(2):237-47.
719 11. Adly N, et al. Ciliary genes TBC1D32/C6orf170 and SCLT1 are mutated in patients with OFD type
720 IX. *Hum Mutat.* 2014;35(1):36-40.
721 12. Kostiuk V, Khokha MK. Xenopus as a platform for discovery of genes relevant to human disease. *Curr*
722 *Top Dev Biol.* 2021;145:277-312.
723 13. Zahn N, et al. Normal Table of Xenopus development: a new graphical resource. *Development.*
724 2022;149(14).
725 14. Perron M, et al. A novel function for Hedgehog signalling in retinal pigment epithelium differentiation.
726 *Development.* 2003;130(8):1565-77.
727 15. Patnaik SR, et al. Bardet-Biedl Syndrome proteins regulate cilia disassembly during tissue maturation.
728 *Cellular and molecular life sciences : CMLS.* 2019;76(4):757-75.
729 16. Doornbos C, et al. Cell-based assay for ciliopathy patients to improve accurate diagnosis using
730 ALPACA. *Eur J Hum Genet.* 2021;29(11):1677-89.
731 17. Muhlhans J, et al. The centrosomal protein pericentrin identified at the basal body complex of the
732 connecting cilium in mouse photoreceptors. *PLoS One.* 2011;6(10):e26496.
733 18. Pazour GJ, et al. The intraflagellar transport protein, IFT88, is essential for vertebrate photoreceptor
734 assembly and maintenance. *J Cell Biol.* 2002;157(1):103-13.
735 19. Shaheen R, et al. Bi-allelic Mutations in FAM149B1 Cause Abnormal Primary Cilium and a Range of
736 Ciliopathy Phenotypes in Humans. *Am J Hum Genet.* 2019;104(4):731-7.
737 20. Assou S, et al. Recurrent Genetic Abnormalities in Human Pluripotent Stem Cells: Definition and
738 Routine Detection in Culture Supernatant by Targeted Droplet Digital PCR. *Stem Cell Reports.*
739 2020;14(1):1-8.
740 21. Schneider S, et al. Loss of Ciliary Gene Bbs8 Results in Physiological Defects in the Retinal Pigment
741 Epithelium. *Front Cell Dev Biol.* 2021;9:607121.
742 22. Zeisberg M, Neilson EG. Biomarkers for epithelial-mesenchymal transitions. *J Clin Invest.*
743 2009;119(6):1429-37.
744 23. Zhou M, et al. Role of Epithelial-Mesenchymal Transition in Retinal Pigment Epithelium Dysfunction.
745 *Front Cell Dev Biol.* 2020;8:501.
746 24. Lenis TL, et al. Expression of ABCA4 in the retinal pigment epithelium and its implications for
747 Stargardt macular degeneration. *Proc Natl Acad Sci U S A.* 2018;115(47):E11120-E7.

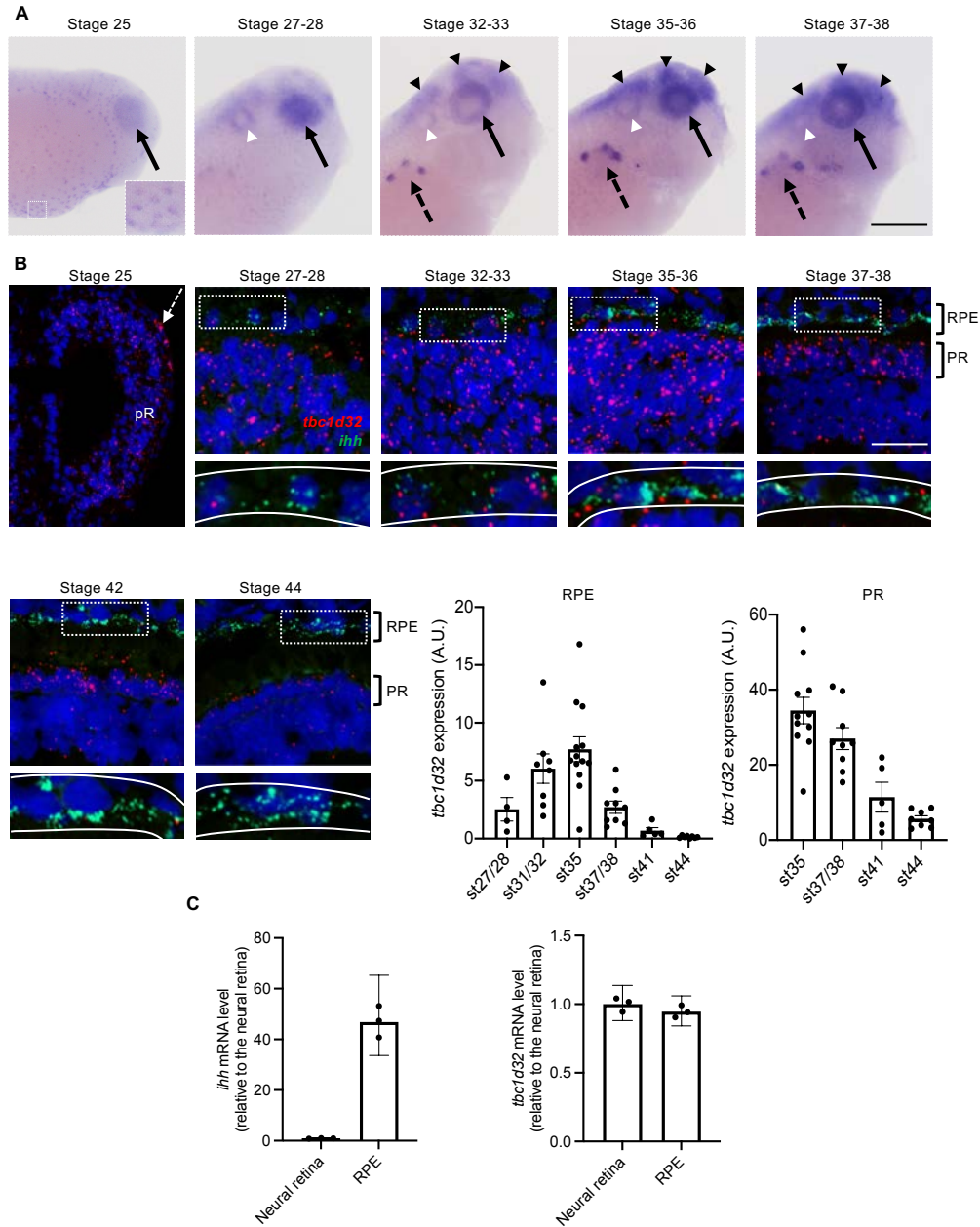
- 748 25. Imanishi Y, et al. Retinosomes: new insights into intracellular managing of hydrophobic substances in
749 lipid bodies. *J Cell Biol.* 2004;166(4):447-53.
- 750 26. Mamaeva D, et al. Novel roles for voltage-gated T-type Ca(2+) and CIC-2 channels in phagocytosis
751 and angiogenic factor balance identified in human iPSC-derived RPE. *FASEB J.* 2021;35(4):e21406.
- 752 27. Sanjurjo-Soriano C, et al. Retinoic acid delays initial photoreceptor differentiation and results in a
753 highly structured mature retinal organoid. *Stem Cell Res Ther.* 2022;13:478.
- 754 28. Tatour Y, Ben-Yosef T. Syndromic Inherited Retinal Diseases: Genetic, Clinical and Diagnostic
755 Aspects. *Diagnostics (Basel).* 2020;10(10).
- 756 29. Talib M, Boon CJF. Retinal Dystrophies and the Road to Treatment: Clinical Requirements and
757 Considerations. *Asia Pac J Ophthalmol (Phila).* 2020;9(3):159-79.
- 758 30. Bruel AL, et al. Fifteen years of research on oral-facial-digital syndromes: from 1 to 16 causal genes.
759 *J Med Genet.* 2017;54(6):371-80.
- 760 31. Pezzella N, et al. OFD1: One gene, several disorders. *Am J Med Genet C Semin Med Genet.*
761 2022;190(1):57-71.
- 762 32. Alsahan N, Alkuraya FS. Confirming TBC1D32-related ciliopathy in humans. *American journal of*
763 *medical genetics Part A.* 2020;182(8):1985-7.
- 764 33. Hietamaki J, et al. Loss-of-Function Variants in TBC1D32 Underlie Syndromic Hypopituitarism. *J*
765 *Clin Endocrinol Metab.* 2020;105(6).
- 766 34. Monies D, et al. Lessons Learned from Large-Scale, First-Tier Clinical Exome Sequencing in a Highly
767 Consanguineous Population. *Am J Hum Genet.* 2019;104(6):1182-201.
- 768 35. Walker RV, et al. Ciliary exclusion of Polycystin-2 promotes kidney cystogenesis in an autosomal
769 dominant polycystic kidney disease model. *Nature communications.* 2019;10(1):4072.
- 770 36. Moon KH, et al. Dysregulation of sonic hedgehog signaling causes hearing loss in ciliopathy mouse
771 models. *Elife.* 2020;9.
- 772 37. Marlhens F, et al. Mutations in RPE65 cause Leber's congenital amaurosis. *Nat Genet.* 1997;17:139-
773 41.
- 774 38. Klettner AK. In: Klettner AK, and Dithmar S eds. *Retinal Pigment Epithelium in Health and Disease.*
775 Switzerland: Springer Nature; 2020:85-100.
- 776 39. Keeling J, et al. Cellular Mechanisms of Ciliary Length Control. *Cells.* 2016;5(1).
- 777 40. Bujakowska KM, et al. Mutations in IFT172 cause isolated retinal degeneration and Bardet-Biedl
778 syndrome. *Hum Mol Genet.* 2015;24(1):230-42.
- 779 41. Halbritter J, et al. Defects in the IFT-B component IFT172 cause Jeune and Mainzer-Saldino
780 syndromes in humans. *Am J Hum Genet.* 2013;93(5):915-25.
- 781 42. Rachel RA, et al. Photoreceptor sensory cilia and ciliopathies: focus on CEP290, RPGR and their
782 interacting proteins. *Cilia.* 2012;1(1):22.
- 783 43. Barny I, et al. AON-Mediated Exon Skipping to Bypass Protein Truncation in Retinal Dystrophies
784 Due to the Recurrent CEP290 c.4723A > T Mutation. Fact or Fiction? *Genes (Basel).* 2019;10(5).
- 785 44. Kruczek K, et al. In vitro modeling and rescue of ciliopathy associated with IQCB1/NPHP5 mutations
786 using patient-derived cells. *Stem Cell Reports.* 2022;17(10):2172-86.
- 787 45. van der Wal T, van Amerongen R. Walking the tight wire between cell adhesion and WNT signalling:
788 a balancing act for beta-catenin. *Open Biol.* 2020;10(12):200267.
- 789 46. Veland IR, et al. Primary cilia and signaling pathways in mammalian development, health and disease.
790 *Nephron Physiol.* 2009;111(3):p39-53.
- 791 47. Liu H, et al. Ciliary signalling in cancer. *Nat Rev Cancer.* 2018;18(8):511-24.
- 792 48. Wang C, et al. Centrosomal protein Dzip11 binds Cby, promotes ciliary bud formation, and acts
793 redundantly with Bromi to regulate ciliogenesis in the mouse. *Development.* 2018;145(6).
- 794 49. Satoda Y, et al. BROMI/TBC1D32 together with CCRK/CDK20 and FAM149B1/JBTS36 contributes
795 to intraflagellar transport turnaround involving ICK/CILK1. *Mol Biol Cell.* 2022;33(9):ar79.
- 796 50. Piro-Megy C, et al. Dominant mutations in mtDNA maintenance gene SSBP1 cause optic atrophy and
797 foveopathy. *J Clin Invest.* 2020;130(1):143-56.

- 798 51. Azhar Baig HM, et al. Genetic Analysis of Consanguineous Pakistani Families with Congenital
799 Stationary Night Blindness. *Ophthalmic research*. 2022;65(1):104-10.
- 800 52. Thompson R, et al. RD-Connect: an integrated platform connecting databases, registries, biobanks and
801 clinical bioinformatics for rare disease research. *J Gen Intern Med*. 2014;29 Suppl 3:S780-7.
- 802 53. Torriano S, et al. Pathogenicity of a novel missense variant associated with choroideremia and its
803 impact on gene replacement therapy. *Hum Mol Genet*. 2017;26(18):3573-84.
- 804 54. Erkilic N, et al. Generation of a human iPSC line, INMi004-A, with a point mutation in CRX
805 associated with autosomal dominant Leber congenital amaurosis. *Stem Cell Res*. 2019;38:101476.
- 806 55. Sanjurjo-Soriano C, et al. *USH2A* variants causing retinitis pigmentosa or Usher syndrome provoke
807 differential retinal phenotypes in disease-specific organoids. *HGG Adv*. 2023;4(4):100229.
- 808

809 **Figure Legends**



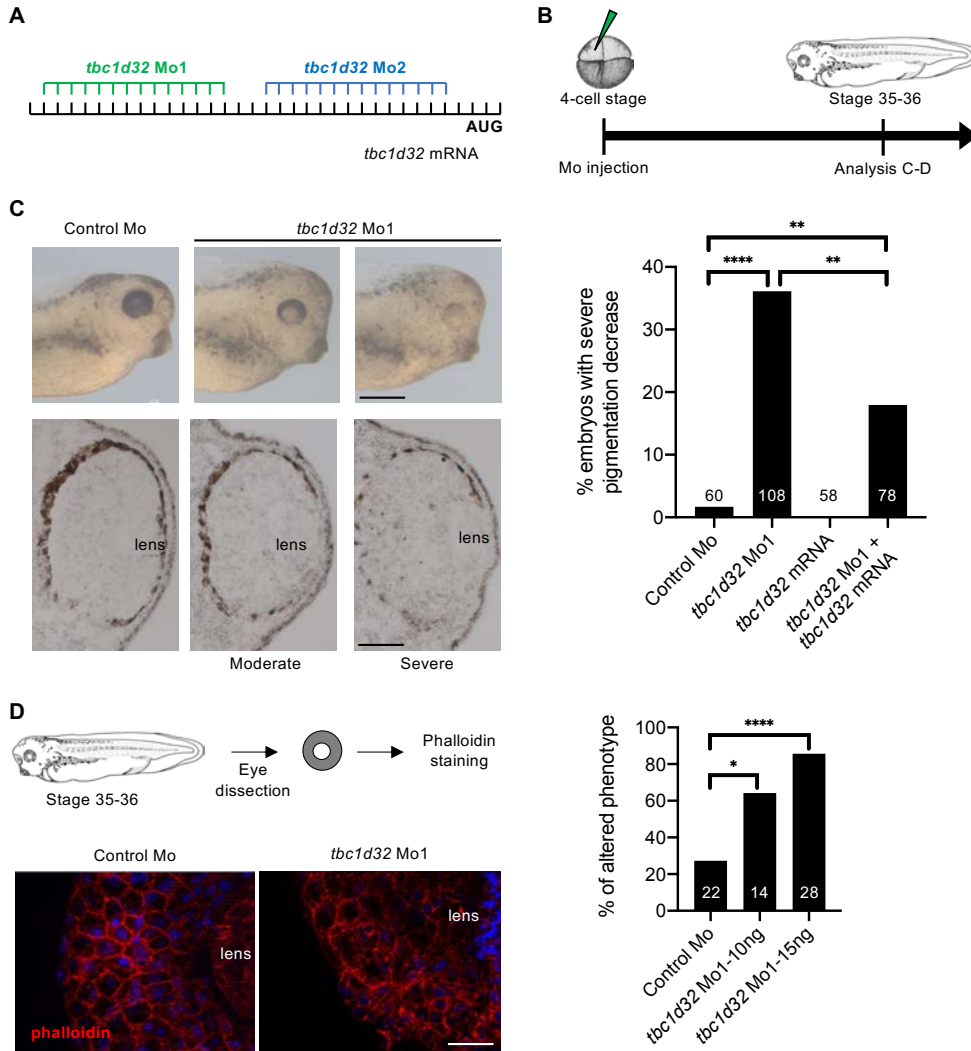
810
811 **Figure 1. Multimodal imaging of the patients.** Patient 1: **A)** Colour fundus photograph showing pallor of
812 the optic nerve head and reduced caliber of the retinal vessels. Note the abnormal visibility of the choroidal
813 vessels due to RPE damage in the midperiphery. **B)** SW-FAF showing a parafoveal ring characteristic of
814 RP (white arrows). **C)** SD-OCT macular scan showing preserved segmentation in the foveal area with
815 peripheral loss of the ellipsoid line nasal to the fovea (white arrow). Patient 2: **D)** Color fundus photograph
816 showing increased choroidal visibility beyond the temporal vascular arcades. Inset: pigment accumulation
817 in the superior retinal periphery. **E)** SW-FAF showing a relatively preserved intensity within the macular
818 region and loss of the signal beyond the temporal vascular arcades. An incomplete hyper-autofluorescent
819 ring is visible in the temporal parafoveal region (yellow arrow). **F)** SD-OCT scan along the horizontal
820 meridian through the fovea showing preservation of retinal layers in the central macula and gradual
821 disappearance of photoreceptor layers with increasing eccentricity in the temporal direction. The white
822 arrow indicates the beginning of the disappearance of the EZ line. Patient 3: **G, H)** Colour fundus imaging
823 of both eyes showing peripheral retinal bone spicules (blue arrows), papillary pallor and evident atrophy of
824 the RPE-choriocapillaris complex except in the macular area (delineated by white arrows). **I)** SD-OCT
825 macular scan showing an ellipsoid line only visible beneath the fovea (between white arrows).



826

827 **Figure 2. *tbc1d32* expression during *Xenopus* development and retinogenesis.** A) Lateral views of
 828 *Xenopus* embryo heads (anterior to the right) following *tbc1d32* whole-mount *in situ* hybridization.
 829 Enlargement: at stage 25, epidermal cells are stained. *tbc1d32* expression is also detected in the eye (black
 830 arrows), and later in the pronephric nephrostomes (black dotted arrows), the brain (black arrowheads) and
 831 the otic vesicle (white arrowheads). **B**) RNAscope *in situ* hybridizations for *tbc1d32* and *ihh* on cryostat
 832 sections. A region of RPE cells, delineated by white dotted boxes in the upper panels, is enlarged in the
 833 lower panels where the RPE layer is outlined with white lines. Scatter plots with bars represent the

834 quantification of *tbc1d32* expression in the RPE or in the photoreceptor layer at each stage (st). Data are
835 represented as mean \pm SEM. Each dot represents one retina. AU: arbitrary units, pR: presumptive retina,
836 RPE: retinal pigment epithelium. PR: photoreceptors. Scale bars = 400 μ m in A, 50 μ m in B. C) qPCR
837 analysis of *ihh* and *tbc1d32* expression in neural retina and RPE tissues, dissected at stage 35-36. *ihh* serves
838 as a specific RPE marker. Data are represented as geometric mean with 95% CI; n = 3 technical replicates.
839



840

841 **Figure 3. *Xenopus* RPE phenotype following *tbc1d32* knockdown.** A) Mo1 and Mo2 target sequences

842 located in the 5'UTR of *tbc1d32* mRNA. B) Diagram of the experimental design. C) Upper panels, lateral

843 views of one control and two morphant embryo heads with moderate and severe phenotypes (anterior to the

844 right). Lower panels, transverse retinal sections of control and morphant embryos (dorsal side up). The

845 histogram represents the percentage of embryos with a severe decrease in pigmentation among control

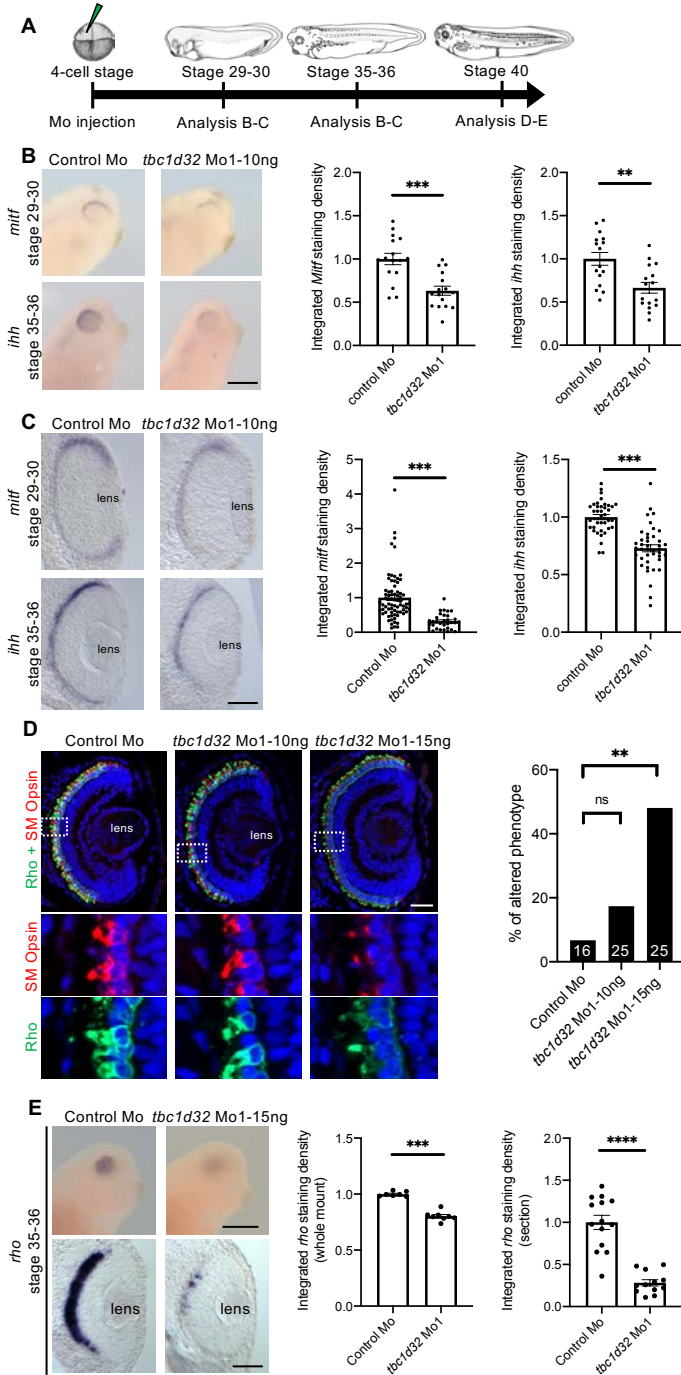
846 (control Mo), morphant (*tbc1d32* Mo1), *tbc1d32* mRNA-injected, and *tbc1d32* Mo1/*tbc1d32* mRNA co-

847 injected, groups. The total number of embryos analyzed per condition is indicated in each bar. **p<0.01;

848 ****p<0.0001; Fisher's exact test. D) Phalloidin staining of filamentous actin on dissected eyes of control

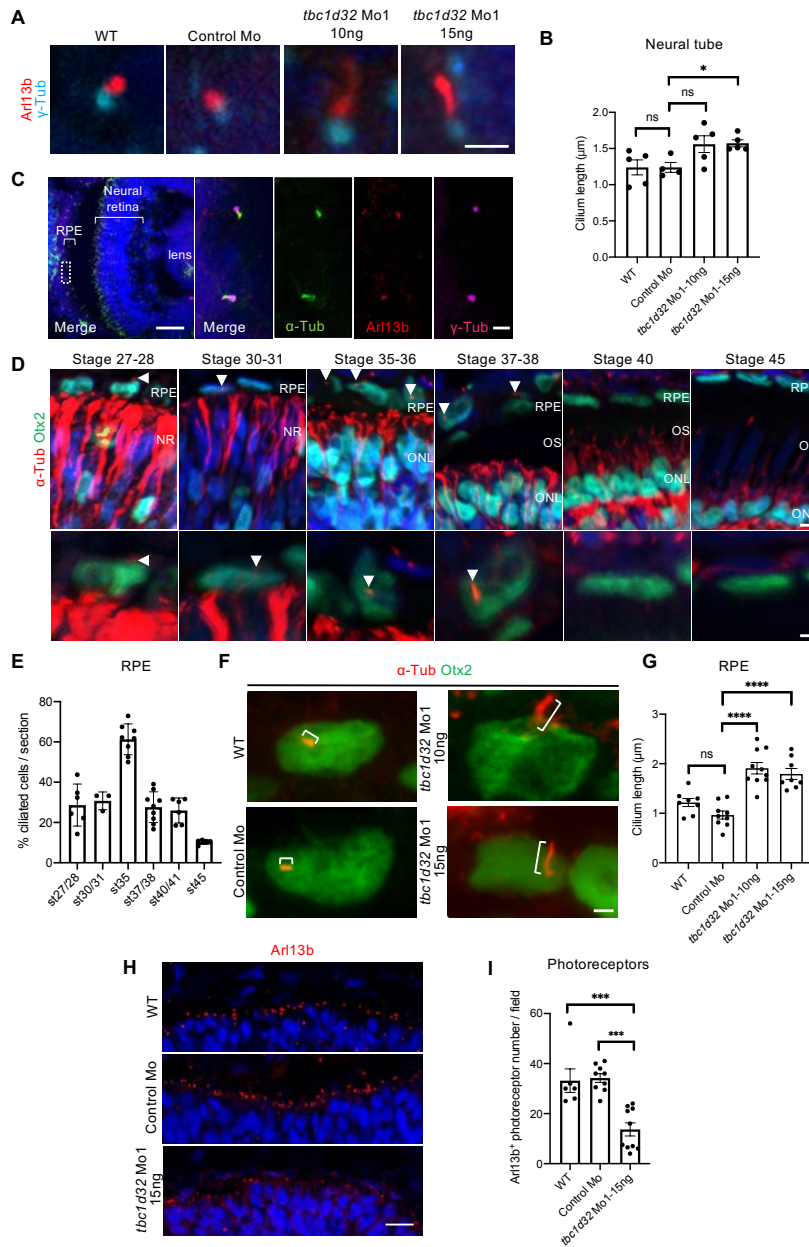
849 or morphant *Xenopus* embryos. The histogram represents the proportion of eyes with an altered distribution

850 of F-actin for each condition. The total number of eyes analyzed per condition is indicated in each bar.
851 * $p < 0.05$; **** $p < 0.0001$; Fisher's exact test. Scale bars = 400 μm for whole mounts and 60 μm for sections
852 in C, and 20 μm in D.
853



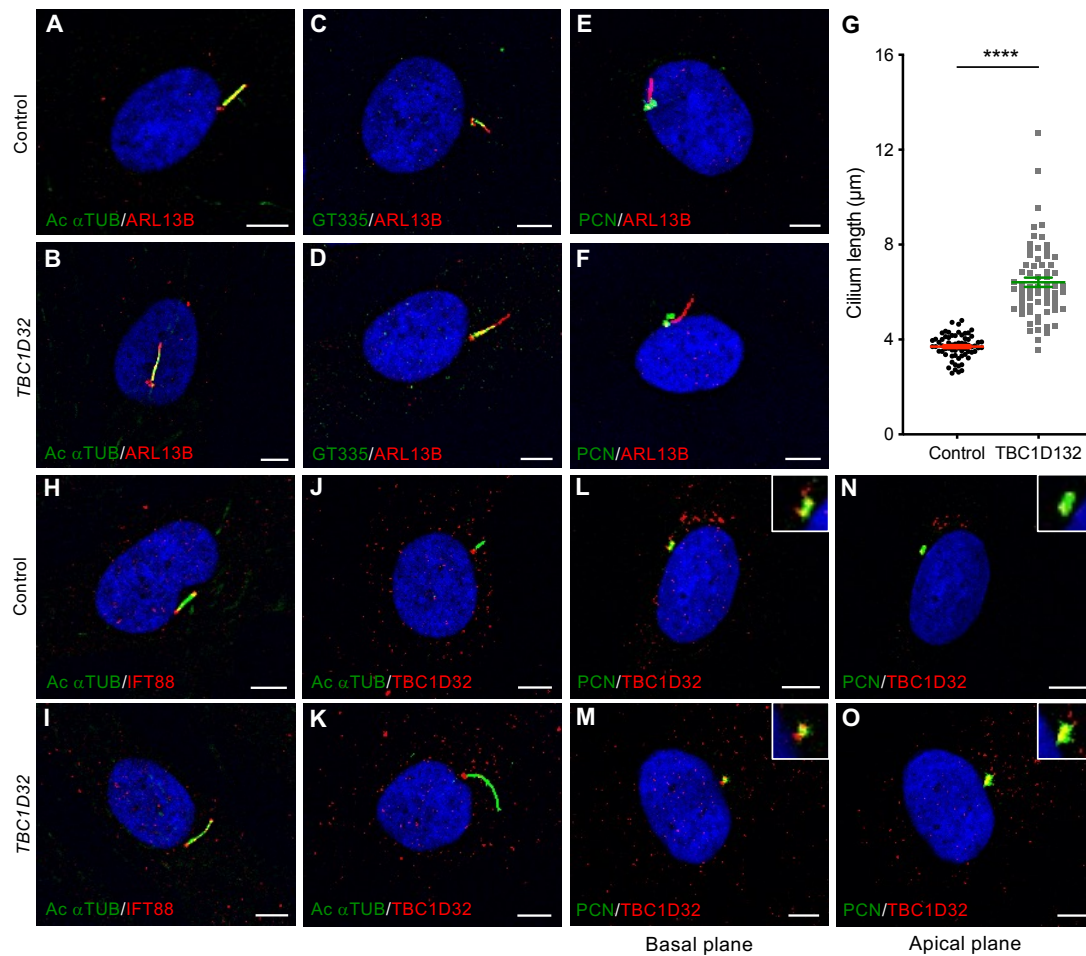
854
 855 **Figure 4. *Xenopus* RPE and photoreceptor marker expression following *tbc1d32* knockdown.** A)
 856 Diagram of the experimental design. Whole mount (B) or retinal sections (C) following *in situ* hybridization
 857 against *mitf* or *ihh*, respectively, on embryos injected with control Mo or *tbc1d32* Mo1. Scatter plots
 858 represent the quantification of the integrated density of the staining per eye relative to control Mo; each dot
 859 corresponds to one eye or one section, respectively. D) Rho and S+M Opsin immunolabelling on retinal

860 sections of embryos injected with control Mo or embryos injected with 2 doses of *tbc1d32* Mo1 (10 or 15
861 ng). Lower panels, enlargement of the areas indicated by white dashed boxes in the upper panels. The
862 histogram represents the proportion of eyes with altered staining of Rho and S+M Opsin for each condition.
863 The number of eyes analyzed per condition is indicated in each bar. E) Upper panels, whole mount *in situ*
864 hybridization against *rhodopsin* (*rho*) in embryos injected with control Mo or *tbc1d32* Mo1. Lower panels,
865 transverse retinal sections of control and morphant embryos. The scatter plots represent the quantification
866 of the integrated density of *rho* staining relative to control Mo; each dot corresponds to one eye (left) or
867 one section (right). For all scatter plots, data are represented as mean \pm SEM. ns: non-significant; * $p < 0.05$;
868 ** $p < 0.01$; *** $p < 0.001$; **** $p < 0.0001$; Fisher's exact test (D); Mann and Whitney test (B, C, and E). Scale
869 bars = 400 μm in B, 40 μm in C and E, 400 μm for whole mount and 40 μm for sections.
870



871
 872 **Figure 5. *Xenopus* ciliogenesis following *tbc1d32* knockdown.** A) Arl13b and γ -Tubulin (γ -Tub)
 873 immunolabelling on neural tube sections of stage 35-36 wild-type (WT), control Mo, or *tbc1d32* Mo1
 874 embryos. B) Scatter plot shows the mean length of neural tube cilia. Each dot corresponds to the mean
 875 length for one embryo. C) Immunolabelling of cilia markers, acetylated α -Tubulin (α -Tub), Arl13b, and γ -

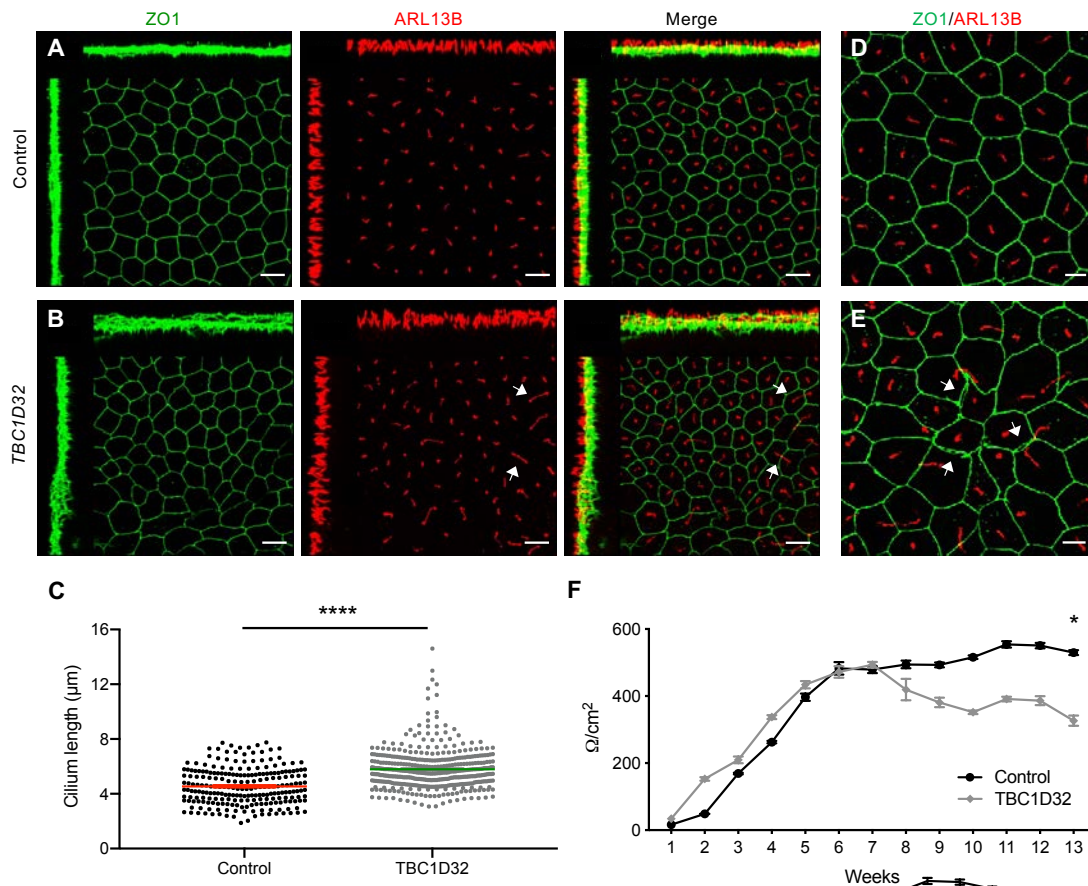
876 Tub, on retinal sections of stage 35-36 WT embryo. The right panels show an enlargement of the area
877 delineated by a white dotted box in the left panel. **D)** α -Tub immunolabelling of RPE cilia (arrowheads) at
878 different stages. Sections are co-stained with Otx2 to identify RPE cells, which are enlarged in the lower
879 panels. NR: neural retina, ONL: outer nuclear layer, OS: outer segment. **E)** Proportion of ciliated cells
880 among RPE cells at different stages (st). **F)** α -Tub and Otx2 immunolabelling showing primary RPE cilia
881 (brackets) on retinal sections of stage 35 WT, control Mo or *tbc1d32* Mo1 embryos. **G)** Scatter plot with
882 bars showing the mean cilia length in RPE cells. Each dot corresponds to the mean length for one embryo.
883 **H)** Immunolabelling of Arl13b showing the photoreceptor connective cilium on retinal sections of stage 35
884 WT, control Mo or *tbc1d32* Mo1 embryos. **I)** The scatter plot shows the mean number of Arl13⁺ ciliated
885 photoreceptors in one field of the central retina. Each dot corresponds to one embryo. All data are
886 represented as mean \pm SEM. ns: non-significant, * $p < 0.05$, *** $p < 0.001$, **** $p < 0.0001$; Mann and Whitney
887 test. Scale bars = 2 μ m in A, 50 μ m and 2 μ m for enlargements in C, 5 μ m and 2 μ m for enlargements in D,
888 25 μ m in H.
889



890
891

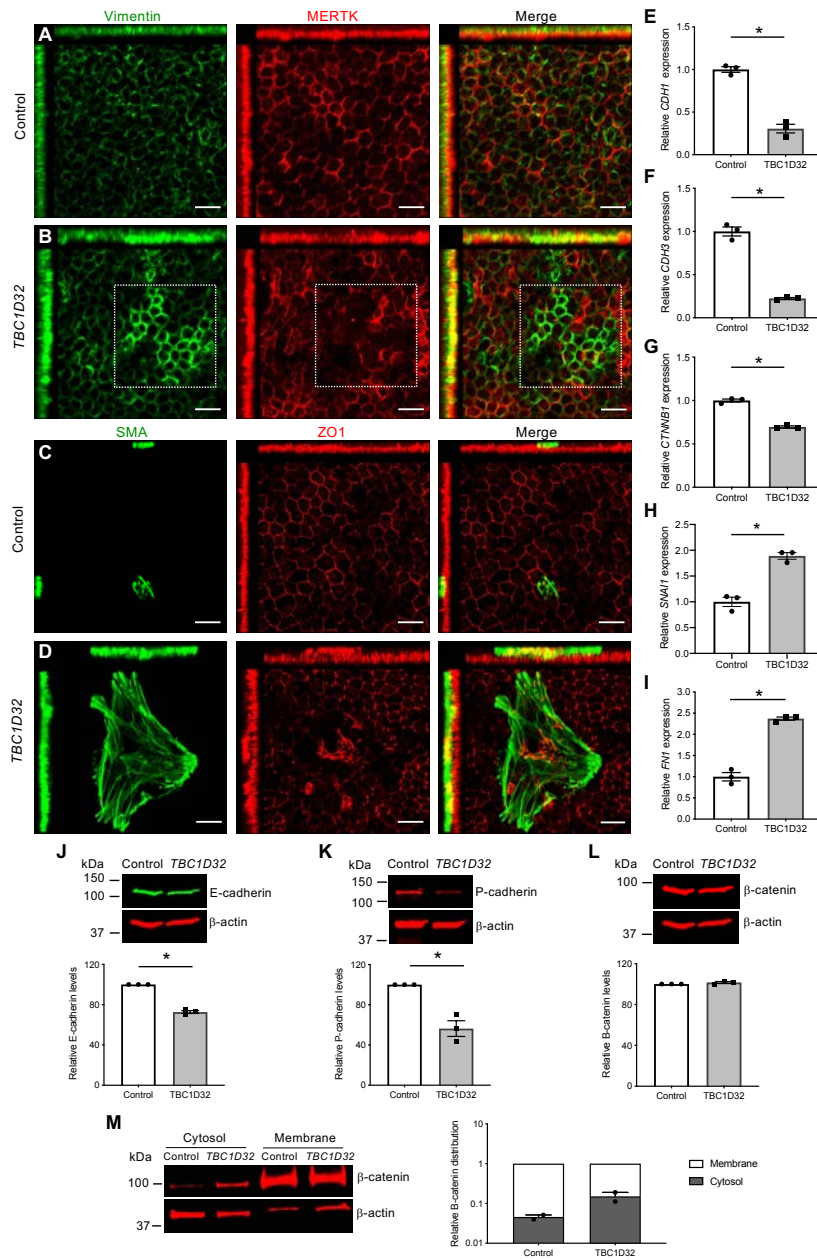
892 **Figure 6. Morphology of the primary cilium in human fibroblasts.** IF studies and single plane confocal
893 imaging to assay ciliogenesis in control (A, C, E) and *TBC1D32* (B, D, E) fibroblasts with antibodies
894 directed against ARL13B and acetylated α -tubulin (Ac α TUB; A, B); GT335 (C, D) and PCN (E, F). G
895 Quantification of cilium length in control and *TBC1D32* fibroblasts. Data are represented as mean \pm SEM;
896 $n = 66$ cells; **** $p < 0.0001$; Student's t-test. IF studies to assay intraflagellar transport in control (H) and
897 *TBC1D32* (I) fibroblasts with antibodies directed against IFT88 and Ac α TUB. IF studies in control (J) and
898 *TBC1D32* (K) fibroblasts to assay the localization of TBC132 in relation to Ac α TUB. IF studies in control
899 (L, N) and *TBC1D32* (M, O) fibroblasts to assay the localization of TBC1D32 in relation to PCN in a basal
900 (L, M) and apical (N, O) plane. Insets show magnification of the labelled basal bodies/centrosomes in each
901 panel. Scale bars = 5 μ m.

902



903
 904
 905
 906
 907
 908
 909
 910
 911
 912
 913
 914
 915

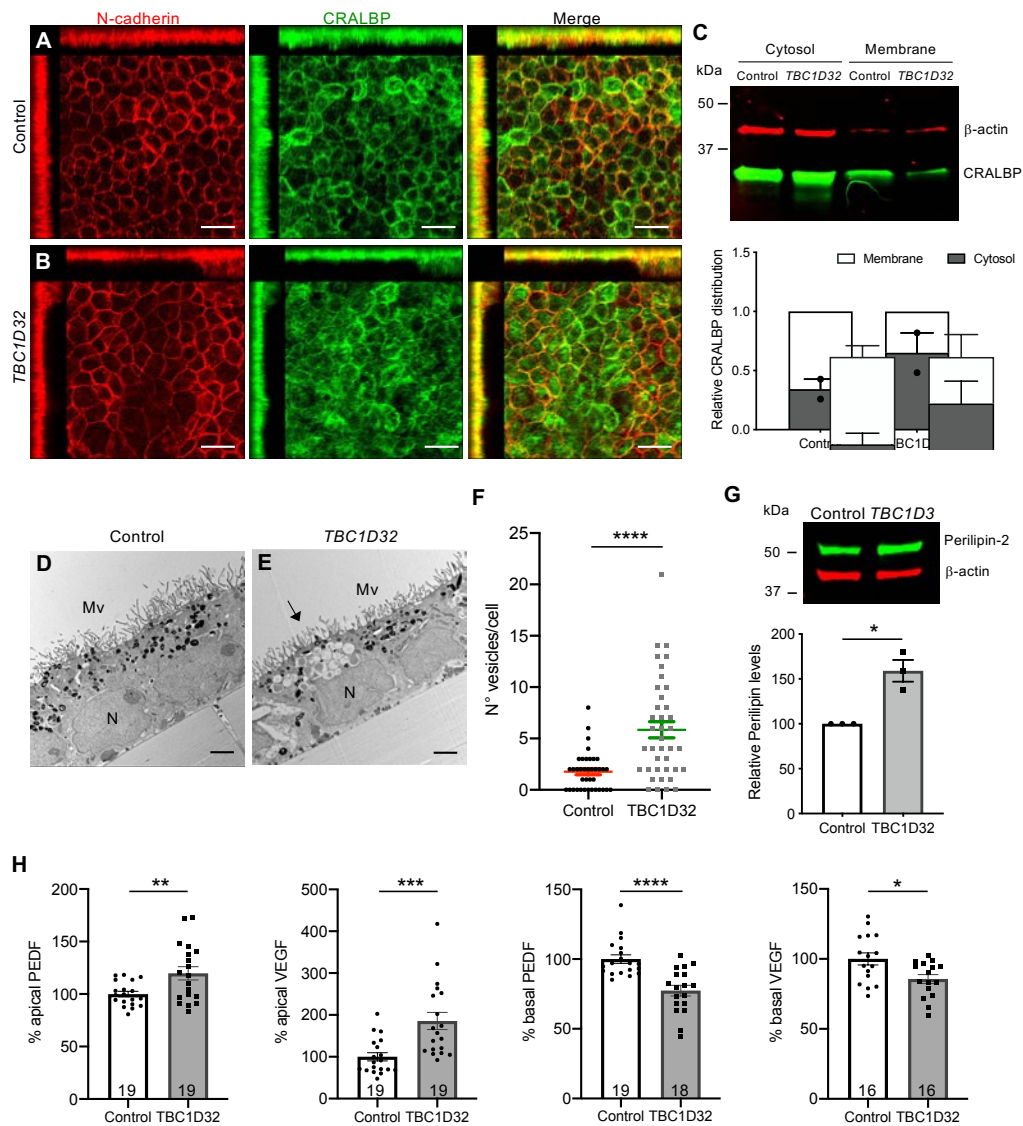
Figure 7. Morphology of the human iPSC-derived RPE. IF studies and maximum intensity projection (MIP) confocal imaging of control (A) and *TBC1D32* (B) iPSC-derived RPE using antibodies directed against ZO1 and ARL13. White arrows indicate elongated cilia. The disrupted *TBC1D32* RPE monolayer can be seen on the orthogonal planes as compared to control. Scale bars = 10 μm. C) Quantification of the cilium length in control (n= 229 cells) and *TBC1D32* iPSC-derived RPE (n= 416 cells). Data are represented as mean ± SEM; ****p<0.0001; Student's t-test. D) Higher magnification of control iPSC-derived RPE showing the regular cobblestone morphology and cilia length. E) Higher magnification of *TBC1D32* RPE showing irregularly-shaped cells, separated tight junctions (white arrows) and ZO1 aggregates. Scale bars = 5 μm. F) Weekly TER measurements expressed in Ω/cm² in control (black line) and *TBC1D32* (grey line) iPSC-derived RPE. Data are represented as mean ± SEM; *p<0.05; n = 4 inserts; Mann and Whitney test.



916

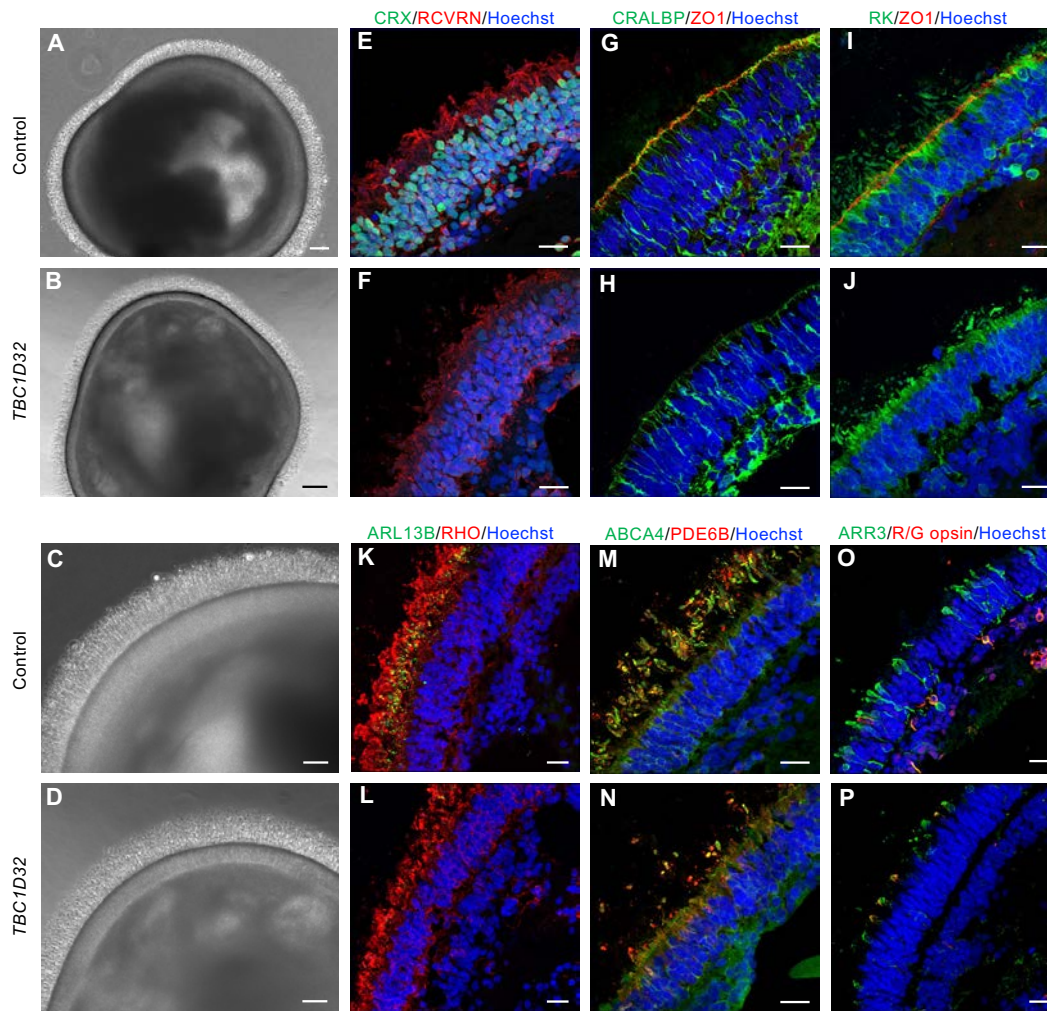
917 **Figure 8. EMT-like phenotype in human *TBC1D32* iPSC-derived RPE.** IF studies and MIP confocal
 918 imaging of control (A) and *TBC1D32* (B) iPSC-derived RPE using antibodies directed against vimentin
 919 and MERTK. The boxed area in B indicates areas of upregulated vimentin and disrupted MERTK
 920 expression. Scale bars = 10 μm. IF studies and MIP confocal imaging of control (C) and *TBC1D32* (D)
 921 iPSC-derived RPE using antibodies directed against SMA and ZO1. Scale bars = 20 μm. qPCR analysis of

922 *CDH1* (**E**), *CDH3* (**F**), *CTNNB1* (**G**), *SNAI1* (**H**) and *FNI* (**I**) in control and *TBC1D32* RPE. Data are
923 represented as mean \pm SEM; n = 3 technical replicates; *p<0.05; Mann and Whitney test. Representative
924 western blot analysis of E-cadherin (**J**), P-cadherin (**K**) and β -catenin (**L**) expression and quantification
925 relative to the β -actin loading control; the same membrane was hybridized with two different primary
926 antibodies in panels J and L. Data represented as mean \pm SEM; n = 3 blots; *p<0.05. **M**) Representative
927 western blot analysis and quantification of two independent blots of β -catenin distribution in the cytosol
928 versus membrane fractions of control and *TBC1D32* iPSC-derived RPE relative to the β -actin loading
929 control and displayed on a logarithmic scale. Data are represented as mean \pm SEM.
930



931
 932 **Figure 9. Retinosome accumulation and altered secretion in human *TBC1D32* iPSC-derived RPE.** IF
 933 studies and MIP confocal imaging of control (A) and *TBC1D32* (B) iPSC-derived RPE using antibodies
 934 directed against N-cadherin and CRALBP. Redistribution of N-cadherin and CRALBP can be seen on the
 935 orthogonal planes. Scale bars = 10 μ m. C) Representative western blot analysis and quantification of two
 936 independent blots of CRALBP distribution in the cytosol versus membrane fractions of control and
 937 *TBC1D32* iPSC-derived RPE relative to the β -actin loading control. Data represented as mean \pm SEM. TEM
 938 of control (D) and *TBC1D32* (E) iPSC-derived RPE showing apical microvilli (MV), basal nuclei (N),
 939 pigmented melanosomes and vesicles corresponding to lipid droplets (black arrow). Scale bar = 2 μ m. F)
 940 Quantification of the number of vesicles per cell in control (n = 38 cells) and *TBC1D32* (n = 39 cells) RPE.
 941 Data are represented as mean \pm SEM; ****p < 0.0001; Student's t-test. G) Representative western blot

942 analysis of perilipin expression and quantification relative to the β -actin loading control. Data represented
943 as mean \pm SEM. n = 3 blots; *p<0.05. **H)** ELISA of PEDF and VEGF secretion in apical and basal chambers
944 of control and TBC1D32 RPE cultured on transwell membrane inserts. Data are expressed as a percentage
945 of control; *p<0.05; **p<0.01; ***p<0.001; ****p<0.0001; the number of samples are indicated within
946 bars. Student's t-test.
947



948
 949 **Figure 10. Morphology of human iPSC-derived retinal organoids.** Bright-field microscopy of control
 950 (A) and *TBC1D32* (B) retinal organoids at day 225 of differentiation showing the brush border. Scale bars
 951 = 100 μm . Higher magnification of the ONL of control (C) and *TBC1D32* (D) organoids. Scale bars = 50
 952 μm . IF studies and MIP confocal imaging of control (E,G,I) and *TBC1D32* (F,H,J) organoids with
 953 antibodies directed to CRX and RCVRN (E,F) to assay general photoreceptor morphology, CRALBP and
 954 ZO1 to assay the OLM (G,H), and RK and ZO1 to assay the prolongation of the IS and OS (I,J). IF studies
 955 of control (K,M,O) and *TBC1D32* (L,N,P) organoids with antibodies directed to ARL13B and RHO (K,L)
 956 to assay the CC and prolongation of the OS, ABCA4 and PDE6B (M,N) to assay the OS of rods and/or
 957 cones, and ARR3 and (in red) (O,P) to assay the cones. All nuclei are labelled with Hoechst. Scale bars =
 958 20 μm .